

A Study of the Multi-frequency Polarization Pulse Profiles of Millisecond Pulsars

S. Dai^{1,2}, G. Hobbs¹, R. N. Manchester¹, M. Kerr¹, R. Shannon¹, W. van Straten³, M. Bailes³, N. D. R. Bhat⁴, S. Burke-Spolaor⁵, W. A. Coles⁶, S. Johnston¹, M. J. Keith⁷, Y. Levin⁸, A. Mata⁹, S. Osłowski^{10,11}, D. Reardon^{8,1}, V. Ravi¹², J. M. Sarkissian¹³, C. Tiburzi^{14,15,1}, L. Toomey¹, H. G. Wang^{16,1}, J.-B. Wang¹⁷, L. Wen¹⁸, R. X. Xu^{2,19}, W. M. Yan¹⁷, X.-J. Zhu¹⁸

¹CSIRO Astronomy and Space Science, Australia Telescope National Facility, Box 76 Epping NSW 1710, Australia

²School of Physics and State Key Laboratory of Nuclear Physics and Technology, Peking University, Beijing 100871, China

³Centre for Astrophysics and Supercomputing, Swinburne University of Technology, PO Box 218, Hawthorn, VIC 3122, Australia

⁴International Centre for Radio Astronomy Research, Curtin University, Bentley, WA 6102, Australia

⁵Department of Astronomy, California Institute of Technology, Pasadena, CA 91125, USA

⁶Department of Electrical and Computer Engineering, University of California, San Diego, La Jolla, CA 92093, USA

⁷Jodrell Bank Centre for Astrophysics, University of Manchester, M13 9PL, UK

⁸School of Physics, Monash University, PO Box 27 Clayton, VIC 3800, Australia

⁹Center for Advanced Radio Astronomy, University of Texas, Rio Grande Valley, Brownsville, TX 78520, USA

¹⁰Max-Planck-Institut für Radioastronomie, Auf dem Hügel 69, D-53121 Bonn, Germany

¹¹Department of Physics, Universität Bielefeld Universitätsstr. 25 D-33615 Bielefeld, Germany

¹²School of Physics, University of Melbourne, Parkville, VIC 3010, Australia

¹³CSIRO Astronomy and Space Science, Parkes Observatory, Box 276, Parkes NSW 2870, Australia

¹⁴INAF-Osservatorio Astronomico di Cagliari, Via della Scienza, I-09047 Selargius (CA), Italy

¹⁵Dipartimento di Fisica, Università di Cagliari, Cittadella Universitaria, I-09042 Monserrato (CA), Italy

¹⁶School of Physics and Electronic Engineering, Guangzhou University, 510006 Guangzhou, China

¹⁷Xinjiang Astronomical Observatory, Chinese Academy of Sciences, 150 Science 1-Street, Urumqi, Xinjiang 830011, China

¹⁸Department of Physics, University of Western Australia, Crawley, WA 6009, Australia

¹⁹Kavli Institute for Astronomy and Astrophysics, Peking University, Beijing 100871, China

22 November 2014

ABSTRACT

We present high signal-to-noise ratio, multi-frequency polarization profiles for 24 millisecond pulsars that are being observed as part of the Parkes Pulsar Timing Array (PPTA) project. The pulsars are observed in three bands, centered close to 730, 1400 and 3100 MHz, using a dual-band 10 cm/50 cm receiver and the central beam of the 20 cm multibeam receiver. Observations spanning many years have been carefully calibrated and summed to produce high S/N profiles. This allows us to study the individual profile components and how they evolve with frequency. We also identify previously undetected profile features. For many pulsars we show that pulse components exist across almost the entire pulse profile. The pulse component widths and component separations follow a complex evolution with frequency; in some cases these parameters increase and in other cases they decrease with increasing frequency. The evolution with frequency of the polarisation properties of the profile is also non-trivial. We provide evidence that the pre- and post-cursors generally have higher fractional linear polarization than the main pulse. We have obtained the spectral index and rotation measure for each pulsar by fitting across all three observing bands. For the majority of pulsars these parameters follow our expectation with a single power-law fitting the spectra and the position angles following the frequency-squared law. However, clear deviations are seen for some pulsars. We also present phase-resolved measurements of the spectral index, fractional linear polarisation and rotation measure. All these properties are shown to vary systematically over the pulse profile.

Key words: pulsars: general

1 INTRODUCTION

Millisecond pulsars (MSPs) are a special subgroup of radio pulsars. Compared with “normal” pulsars, they have much shorter spin periods and smaller spin-down rates, and therefore have larger characteristic ages and weaker implied dipole magnetic fields. The short spin periods and highly stable average pulse shapes of MSPs make them powerful tools to investigate a large variety of astrophysical phenomena. In particular, much recent work has been to search for a gravitational wave background using observations of a large sample of MSPs in a “Pulsar Timing Array” (e.g., Foster & Backer 1990). The Parkes Pulsar Timing Array (PPTA) project (Manchester et al. 2013) regularly observes 24 MSPs. The PPTA search for gravitational waves has been described in other papers including Shannon et al. (2013), Wang et al. (2014) and Zhu et al. (2014).

We have not yet detected gravitational waves. In order to do so we will need to observe a larger set of pulsars, increase the span of the observations and/or to increase the timing precision achieved for each observation. Determining whether it is possible to improve the timing precision and, if so, by how much relies on our understanding of the stability of pulse profiles (e.g., Shannon et al. 2014) and also on the profile frequency evolution and polarization properties. For our work we study the large number of well calibrated, high signal-to-noise ratio (S/N) multi-frequency polarization profiles that have been obtained as part of the PPTA project.

An earlier analysis of the 20 cm pulse profiles from the PPTA sample was published by Yan et al. (2011b). This earlier work is extended in this paper as: (1) we include an extra four pulsars that have recently been added to the PPTA sample; (2) we use more modern pulsar backend instrumentation than was available to Yan et al. (2011b); (3) we use longer data sets enabling higher S/N ratio profiles; and (4) we provide polarization pulse profiles in three independent bands (at 10, 20 and 50 cm). We note that, even though we have mainly the same sample of pulsars as was described by Yan et al. (2011b), our data sets are independent (i.e., no data is in common between this and the earlier publication).

It has been shown that, compared with normal pulsars, the pulse profiles of MSPs are much more complicated and cover a much larger fraction of the pulse period (Yan et al. 2011b). However, the spectra of MSPs and normal pulsars are similar (Toscano et al. 1998; Kramer et al. 1998, 1999a). Both MSPs and normal pulsars often have a high degree of linear polarization and orthogonal mode position angle (PA) jumps (see e.g., Thorsett & Stinebring 1990; Navarro et al. 1997; Stairs et al. 1999; Manchester & Han 2004; Ord et al. 2004). For MSPs the PAs often varies significantly with pulse phase and, in most cases, they do not fit the ‘rotating vector model’ (RVM, Radhakrishnan & Cooke 1969).

To explain the complex pulse profiles, multiple emission cones were proposed and discussed by several authors (Rankin 1993; Kramer 1994; Gupta & Gangadhara 2003). An alternative model suggests that the emission beam of a pulsar is filled with randomly distributed emission patches (Lyne & Manchester 1988; Manchester 1995; Han & Manchester 2001). Based on investigations of the radio and *gamma*-ray beaming properties of both normal pulsars and MSPs, Manchester (2005) and Ravi et al. (2010)

proposed that the radio emission of young and MSPs originates in wide beams from regions high in the pulsar magnetosphere and that features in the radio profile represent caustics in the emission beam pattern.

To date, no simple model exists yet that can describe the observations. This paper is an observationally-based publication that we hope will shed new light on the MSP emission mechanism. We present the new profiles in the various observing bands and describe how they were created. We determine various observationally-derived properties of the profiles (such as spectral indices, polarization fractions, etc.) and study how such parameters vary between pulsars and with frequency. Using these high S/N profiles, we also carry out phase-resolved studies on the spectral index (e.g., Lyne & Manchester 1988; Kramer et al. 1994; Manchester & Han 2004; Chen et al. 2007), linear polarization fraction and rotation measures (RMs) (e.g., Noutsos et al. 2009). The data described here will be used in a subsequent paper to study the stability of the pulse profiles as a function of time. This sample of pulsars has been chosen for high-precision pulsar timing experiments. In a further paper, we will apply new methods (e.g., Pennucci et al. 2014; Liu et al. 2014) to improve our timing precision using frequency-dependent pulse templates. Our data sets are publically available enabling anyone to compare the actual observations with their models of the pulse profiles.

Details of the observation, data processing and data access are given in Section 2. In Section 3, we present the multi-frequency polarization pulse profiles. The pulse widths, flux densities and spectral indices, polarization parameters and rotational measures are presented in Section 4 to 7. A summary of our results and conclusions are given in Section 8.

2 OBSERVATIONS AND ANALYSIS

2.1 Observations

We selected observations from the PPTA project of 24 MSPs. The pulsars are observed regularly, with an approximate observing cadence of three weeks, in three bands centred close to 730 MHz (50 cm), 1400 MHz (20 cm) and 3100 MHz (10 cm), using a dual-band 10 cm/50 cm receiver and the central beam of the 20 cm multibeam receiver. The observing bandwidth was 64, 256 and 1024 MHz respectively for the 50 cm, 20 cm and 10 cm bands. We used both digital polyphase filterbank spectrometers (PDFB4 at 10 cm and PDFB3 at 20 cm) and a coherent dedispersion machine (CASPSR at 50 cm). In Table 1, we summarize the observational parameters for the 24 PPTA MSPs. For each band, we give the number of frequency channels across the band, the number of bins across the pulse period, the total number of observations and the total integration time. In Table 2, we give the basic pulsar parameters from the ATNF Pulsar Catalogue (Manchester et al. 2005). For each observing band, we also give the dispersion smearing and the pulse broadening time caused by scattering (in units of profile bins). The dispersion smearing across each frequency channel is calculated according to,

$$\Delta t_{\text{DM}} \approx 8.30 \times 10^6 \text{ DM } \Delta\nu \nu^{-3} \text{ ms}, \quad (1)$$

where $\Delta\nu$ is the channel width in MHz, ν is the band centre frequency in MHz, and the DM is in units of $\text{cm}^{-3} \text{ pc}$.

The pulse broadening time caused by scattering is estimated according to

$$\tau_d = \frac{1}{2\pi\nu_0}, \quad (2)$$

where ν_0 is the scintillation bandwidth. We calculate the broadening time in the 20 cm band using scintillation bandwidths measured by Keith et al. (2013), and then scale it to the 10 cm and 50 cm bands according to $\tau_d \propto \nu^{-4}$. For MSPs not in the sample of Keith et al. (2013), we estimate the pulse broadening time using the empirical fit from Bhat et al. (2004),

$$\log \tau_d = -6.46 + 0.154 \log \text{DM} + 1.07(\log \text{DM})^2 - (3.86 \pm 0.16) \log \left(\frac{\nu}{1000} \right) \text{ ms}. \quad (3)$$

We note that in Table 2, we only list τ_d values that are ≥ 0.0001 bin and set others as zero.

To calibrate the gain and phase of the receiver system, a linearly polarized broad-band and pulsed calibration signal is injected into the two orthogonal channels through a calibration probe at 45° to the signal probes. The pulsed calibration signal was recorded for 2 min prior to each pulsar observation. Signal amplitudes were placed on a flux density scale using observations of Hydra A, assuming a flux density of 43.1 Jy at 1400 MHz and a spectral index of ~ 0.91 over the PPTA frequency range. All data were recorded using the PSRFITS data format (Hotan et al. 2004) with 1-min subintegrations and the full spectral resolution (for further details see Manchester et al. 2013, and references therein).

2.2 Analysis

The data were processed using the PSRCHIVE software package (Hotan et al. 2004). We removed 5 per cent of the bandpass at each edge and excised data affected by narrow band and impulsive radio-frequency interference for each sub-integration. The polarization was then calibrated by correcting for differential gain and phase between the receptors using the associated calibration files. For 20 cm observations with the Multibeam receiver, we corrected for cross coupling between the feeds through a model derived from observations of PSR J0437–4715 that covered a wide range of parallactic angles (van Straten 2004).

The Stokes parameters are in accordance with the astronomical conventions described by van Straten et al. (2010). Stokes V is defined as $I_{\text{LH}} - I_{\text{RH}}$, using the IEEE definition for sense of circular polarization. The linear polarization L was calculated as $L = (Q^2 + U^2)^{1/2}$, and the noise bias in L was corrected according to Lorimer & Kramer (2005), and the similar bias in $|V|$ was corrected as described in Yan et al. (2011b). The position angles (PAs) of the linear polarization refer to the band central frequency and were calculated as $\psi = 0.5 \tan^{-1}(U/Q)$. They are absolute and measured from celestial north towards east, i.e. counterclockwise on the sky. Errors on the PA values were estimated according to Everett & Weisberg (2001). The baseline region was determined with the mean pulse profile using a default baseline duty cycle of 0.2 (for pulsars that different duty cycles were used, we give the value in their specific comments in the Appendix), and baselines for each of the Stokes parameter profiles were set to zero mean.

In order to add the data in time to form a final mean profile, pulse times of arrival were obtained for each observation using an analytic template based on an existing high S/N pulse profile. The TEMPO2 pulsar timing software package (Hobbs et al. 2006) was then used to fit pulsar spin, astrometric and binary parameters, and also to fit harmonic waves as necessary to give white timing residuals for each pulsar. Finally, the separate observations were summed using this timing model to determine relative phases and form the final Stokes-parameter profiles.

To give the best possible S/N in the polarization pulse profiles, the individual observation profiles were weighted by their $(S/\text{N})^2$ when forming the average profile. As many of the pulsars scintillate strongly, this weighting implies that, for a few pulsars, we are dominated by a few individual observations that have a high S/N. As discussed in Section 5 this can affect measurements of the spectral index, fractional polarizations and RMs. Also, if the pulse profile varies with flux density (for instance, as seen for PSR J0437–4715 by Oslowski et al. 2014) then this weighted profile will be biased towards the profile shape at high flux density. We therefore have also produced profiles that were averaged together with the only weighting being the observation time.

To form mean polarization profiles, the Faraday rotation across the band must be corrected. According to Yan et al. (2011a), the interstellar RMs of PPTA MSPs are stable, and for our initial analysis we used the best-available interstellar RM values for our sample (Keith et al. 2011; Yan et al. 2011b; Keith et al. 2012; Burgay et al. 2013). To account for the contribution of the Earth's ionosphere, we used the International Reference Ionosphere (IRI) model¹.

For each MSP, we aligned the average profile in the 10 and 50 cm bands with respect to that in the 20 cm band. The technique we used is described in detail in Taylor (1992), which was originally developed for the measurement of pulse arrival times. We derived the phase shift between profiles and the profile in the 20 cm band in the frequency domain, rotated the profiles and then transformed them back to the time domain. With these aligned three-band profiles, we calculated the phase-resolved spectral indices, fractional linear polarizations and RMs for each MSP. The spectral index was fitted using a power-law of the form $S = S_0 \nu^\alpha$ and the fractional linear polarization was defined as $\langle L \rangle / S$, where $S = \langle I \rangle$ is the total intensity and L is the linear polarization. The RM was obtained by fitting the PA across bands according to $\psi = \text{RM } \lambda^2$, where $\lambda = c/\nu$ is the radio wavelength corresponding to radio frequency ν .

2.3 Data access

The raw data and calibration files used in this paper are available from the Parkes data archive (Hobbs et al. 2011, data.csiro.au). The scripts used to create the results given in this paper and the resulting averaged (weighted and unweighted) profiles are available for public access from XXX.

¹ See <http://iri.gsfc.nasa.gov> for a general description of the IRI.

Table 1. Observational parameters for the 24 PPTA MSPs.

PSR	No. of channels			No. of phase bins			No. of observation epochs			Integration time (h)		
	50 cm	20 cm	10 cm	50 cm	20 cm	10 cm	50 cm	20 cm	10 cm	50 cm	20 cm	10 cm
J0437–4715	256	1024	1024	1024	1024	2048	177	669	281	142.9	502.2	248.8
J0613–0200	256	1024	1024	1024	512	512	64	160	111	66.0	159.3	113.9
J0711–6830	256	1024	1024	1024	1024	1024	72	161	102	65.9	161.1	102.2
J1017–7156	256	2048	2048	1024	256	512	85	135	73	86.5	130.4	76.3
J1022+1001	256	1024	1024	1024	2048	2048	65	148	117	58.4	138.3	110.5
J1024–0719	256	1024	1024	1024	1024	1024	34	112	59	36.1	111.0	61.5
J1045–4509	256	2048	1024	1024	512	1024	63	137	103	42.7	138.9	104.5
J1446–4701	256	512	1024	1024	512	1024	19	50	9	15.2	39.4	8.8
J1545–4550	256	1024	1024	1024	512	1024	15	21	15	13.2	20.6	12.2
J1600–3053	256	1024	1024	1024	512	512	53	139	106	56.6	129.9	108.0
J1603–7202	256	2048	1024	1024	1024	1024	52	131	49	44.4	127.4	50.6
J1643–1224	256	2048	1024	1024	512	1024	53	116	93	53.7	117.0	93.4
J1713+0747	256	1024	1024	1024	1024	1024	66	155	110	67.8	132.0	107.9
J1730–2304	256	1024	1024	1024	1024	2048	57	104	62	51.0	105.8	62.2
J1744–1134	256	512	1024	1024	1024	1024	65	129	96	66.0	126.7	99.5
J1824–2453A	256	2048	1024	1024	256	512	33	88	54	33.0	82.9	53.6
J1832–0836	256	1024	1024	1024	512	1024	12	19	11	9.0	16.9	10.1
J1857+0943	256	1024	1024	1024	1024	1024	54	99	68	27.8	50.9	35.5
J1909–3744	256	1024	1024	1024	512	1024	95	218	138	91.3	191.1	129.4
J1939+2134	256	1024	1024	512	256	256	58	102	91	26.4	49.4	46.0
J2124–3358	256	1024	1024	1024	1024	1024	40	134	78	20.3	68.5	40.5
J2129–5721	256	1024	1024	1024	512	512	59	116	17	31.1	112.6	9.0
J2145–0750	256	1024	1024	1024	2048	2048	70	134	117	65.1	129.3	111.2
J2241–5236	256	1024	1024	1024	512	1024	75	188	93	69.8	152.3	92.9

3 MULTI-FREQUENCY POLARIZATION PROFILES

Our main results are the polarisation profiles for the PPTA pulsars in the three bands. These are shown, for each of the 24 pulsars, in Figures A1 to A24. The left-hand panels show the pulse profile in the 10 cm (top), 20 cm (second panel) and 50 cm (third panel) observing bands. The bottom panel on the left-hand side presents the phase-resolved spectral index. In order to obtain the phase-resolved spectral index, we divided the 10 cm and 20 cm band into four subbands and the 50 cm band into three subbands. We rebinned the profile in each subband into 256 phase bins to gain higher S/N. Only phase bins whose signal exceeds three times of the baseline rms noise are used and we only plot spectral indices whose uncertainty is smaller than one. The red dashed line and the yellow highlighted region represent the mean spectral index and its uncertainty, as presented in the last column of Table 6.

In the right-hand panels we have two panels for each of the 10, 20 and 50 cm bands. The upper panel shows the PA of the linear polarization (in degrees) determined when the linear polarization exceeds four times of the baseline rms noise. The lower panels shows a zoom-in around profile baseline to show weaker profile features. The bottom two panels on the right-hand side show the phase-resolved fractional linear polarization for the three observing bands and the phase-resolved apparent RM. In order to obtain the phase-resolved fractional linear polarization, we rebinned the profile in each

band into 128 phase bins to gain higher S/N and only phase bins whose linear polarization exceeds three times of the baseline rms noise were used. The phase-resolved RMs were obtained with the frequency-averaged profile in each band without any rebinning. Only phase bins whose linear polarization exceeds five times of the baseline rms noise were used, and we only plot RMs whose uncertainty is smaller than 3 rad m⁻². The red dashed line and yellow highlighted region represent the measured RM value and its uncertainty, as described in Section 7

In almost all cases our results are consistent with earlier measurements (such as Ord et al. 2004; Yan et al. 2011b) where these exist. Specific comments on the processing for each individual pulsar and on the comparison with previous work are given below. In particular, we have discovered weak components for PSRs J2145–0750, J1603–7202 and J2241–5236. We also show new details of the PA curves, including new orthogonal transitions for PSRs J0437–4715, J0711–6830, J1643–1224, J2124–3358, J2129–5721 and J2241–5236; and new non-orthogonal transitions for PSRs J1045–4509, J1857+0943 and J2124–3358.

3.1 PSR J0437–4715

Fig. A1 shows the polarization pulse profiles of the strongest PPTA MSP, PSR J0437–4715. We used a baseline duty cycle of 0.05 in our processing. At 20 cm, the S/N of the profile of total intensity is up to ∼ 33,500. Our results are in good agreement with previously published works (Johnston et al.

Table 2. Pulsar parameters for the 24 PPTA MSPs.

PSR	P (ms)	DM (cm ⁻³ pc)	DM smear				τ_d (bins)	
			50 cm	20 cm	10 cm	50 cm	20 cm	10 cm
J0437–4715	5.757	2.64	7.9	0.4	0.3	0.0004	0.0000	0.0000
J0613–0200	3.062	38.78	218.0	5.2	1.8	0.4058	0.0162	0.0006
J0711–6830	5.491	18.41	57.7	2.8	1.0	0.0103	0.0008	0.0000
J1017–7156	2.339	94.22	693.4	4.2	2.9	15.4014	0.3364	0.0287
J1022+1001	16.453	10.25	10.7	1.0	0.4	0.0019	0.0003	0.0000
J1024–0719	5.162	6.49	21.6	1.0	0.4	0.0015	0.0001	0.0000
J1045–4509	7.474	58.17	133.9	1.6	2.2	2.9005	0.1160	0.0088
J1446–4701	2.195	55.83	437.8	21.1	7.3	1.8849	0.0823	0.0070
J1545–4550	3.575	68.39	329.2	7.9	5.5	2.5985	0.1135	0.0097
J1600–3053	3.598	52.33	250.3	6.0	2.1	6.2935	0.2516	0.0096
J1603–7202	14.842	38.05	44.1	1.1	0.7	0.0275	0.0022	0.0001
J1643–1224	4.622	62.41	232.4	2.8	3.9	20.0424	0.8014	0.0610
J1713+0747	4.570	15.99	60.2	2.9	1.0	0.0186	0.0015	0.0001
J1730–2304	8.123	9.62	20.4	1.0	0.7	0.0202	0.0016	0.0001
J1744–1134	4.075	3.14	13.3	1.3	0.2	0.0083	0.0007	0.0000
J1824–2453A	3.054	120.50	675.5	4.1	5.6	26.6882	0.5335	0.0406
J1832–0836	2.719	28.18	178.3	4.3	3.0	0.1321	0.0058	0.0005
J1857+0943	5.362	13.30	42.7	2.1	0.7	0.0691	0.0055	0.0002
J1909–3744	2.947	10.39	60.7	1.5	1.0	0.0187	0.0007	0.0001
J1939+2134	1.558	71.04	392.3	9.4	3.3	0.5451	0.0218	0.0008
J2124–3358	4.931	4.60	16.0	0.8	0.3	0.0004	0.0000	0.0000
J2129–5721	3.726	31.85	147.1	3.5	1.2	0.0320	0.0013	0.0000
J2145–0750	16.052	9.00	9.7	0.9	0.3	0.0007	0.0001	0.0000
J2241–5236	2.187	11.41	89.8	2.1	1.5	0.0126	0.0006	0.0000

1993; Manchester & Johnston 1995; Navarro et al. 1997; Yan et al. 2011b), which presented multiple overlapping components and complex polarization variations across the pulse profile. The overall width is more than 300° in all three bands. The profile of total intensity shows clear frequency development. The main peak has two components with the second component having a steeper spectrum and disappearing at high frequencies. The leading and trailing parts of the main peak have steeper spectral indices. However, the outer edges of the profile have flat spectra. We have tried different baseline duty cycles from 0.1 to 0.05 in our processing and found that the results we present here are not significantly affected. Such features are consistent with the Murchison Widefield Array (MWA) observation at a frequency of 192 MHz, which shows that at low frequencies the central bright component is flanked by multiple outer components (Bhat et al. 2014). The PA curves change dramatically in different bands. While the orthogonal transition close to the main profile peak exists in all three bands, previously reported non-orthogonal transitions at 20 cm are not so clear in the other two bands, and new transitions and discontinuous features can be observed in the 10 cm and 50 cm bands. The phase-resolved spectral indices, fractional linear polarizations and apparent RMs vary dramatically across the profile. Close to phase zero, we observed step changes in the phase-resolved spectral index and apparent RM, which coincide with the change in distribution of phase-resolved electric field magnitude observed by Oslowski et al. (2014).

3.2 PSR J0613–0200

Fig. A2 shows the polarization pulse profiles of PSR J0613–0200. At 20 cm, our results are in good agreement with previously published results (Ord et al. 2004; Yan et al. 2011b). Our high S/N profiles provide more details in the PA curve, and we show that the PA curves are complex and very different in three bands. At 20 cm, the discontinuous PA at the leading edge of the trailing component reported by Yan et al. (2011b) is not observed, and the PA curve seems to be continuous. The main pulse of the profile shows clear frequency evolution, and most significantly, the trailing peak has a very steep spectrum. The trailing peak splits into two peaks at low frequencies as previously observed by Stairs et al. (1999). From the high frequencies to low frequencies, the fractional linear polarization increases, and the trailing component becomes highly linear polarized. At 50 cm, the circular polarization swaps sign compared to higher frequencies. The three main pulse components of the profile clearly have different apparent RMs.

3.3 PSR J0711–6830

Fig. A3 shows the polarization pulse profiles of PSR J0711–6830. We used a baseline duty cycle of 0.05 in our processing. At 20 cm, our results are in good agreement with previously published results (Ord et al. 2004; Yan et al. 2011b). The double-peaked weak component following the second peak is clear. The orthogonal mode transition after the peak of the leading component is confirmed at

20 cm and is seen at 50 cm. However the orthogonal mode transition near the trailing edge of the main peak is not present at 50 cm. The leading component has slightly steeper spectrum than the main pulse. The fractional linear polarization of the main peak decreases significantly with increasing frequency.

3.4 PSR J1017–7156

Fig. A4 shows the polarization pulse profiles of PSR J1017–7156. Our results are in good agreement with, and extend, previously published results (Keith et al. 2012). We show that the PA variations are more complex than was observed in previous work. While the leading and trailing edge of the main pulse has a steeper spectrum compared with the central peak, the trailing component around phase 0.04 has a much flatter spectrum. Both the linear and circular polarisation has multiple components and shows significant evolution with frequency. Especially, the main pulse of the circular polarization seems to be consist of two components and one of them has narrower width and much steeper spectrum.

3.5 PSR J1022+1001

Fig. A5 shows the polarization pulse profiles of PSR J1022+1001. Our results are in good agreement with previously published results (Kramer et al. 1999b; Stairs et al. 1999; Ord et al. 2004; Yan et al. 2011b). At 10 cm, despite of the discontinuity close to phase zero, the PA variation fits the RVM very well. As the frequency decreases, the PA variation departs from the RVM progressively. The spectral indice of two main peaks are significantly different so that the relative strength of the two main peaks evolves dramatically with frequency. While the second peak keeps highly linearly polarized, the first peak depolarizes rapidly. We also see systematic variation of the phase-resolved apparent RMs.

3.6 PSR J1024–0719

Fig. A6 shows the polarization pulse profiles of PSR J1024–0719. We used a baseline duty cycle of 0.05 in our processing. At 20 cm, our results are in good agreement with previously published results (Ord et al. 2004; Yan et al. 2011b). Besides the flat PA curve across the main part of the profile as previously reported, we also show the PAs of the trailing component which increases with phase at 20 cm and 50 cm. The leading component and the trailing component of the profile have much steeper spectra compared with the central peaks. The leading part of the profile is highly linear polarized and has stable RMs. As the fractional linear polarization drops down at the trailing part, the RMs show some variations.

3.7 PSR J1045–4509

Fig. A7 shows the polarization pulse profiles of PSR J1045–4509. At 20 cm, our results are in good agreement with previously published results (Yan et al. 2011b), and confirm that the leading emission is joined to the main pulse by a low-level bridge of emission. We show the complex PA

curve with more detail, and determine the PA of the low-level bridge connecting the leading emission and the main pulse. At the leading edge of the main pulse, there is a non-orthogonal transition rather than a orthogonal transition as suggested by Yan et al. (2011b). The PA of the low-level bridge emission seems to be discontinuous with the rest of the PA variations and could be an orthogonal mode. The pulse profile and its polarization are relatively frequency-independent, apart from an increase in the linear polarization of the trailing component at high frequencies.

3.8 PSR J1446–4701

Fig. A8 shows the polarization pulse profiles of PSR J1446–4701. At 20 cm, our results are generally consistent with previously published results (Keith et al. 2012). The PAs are flat over the main pulse, but show variations over the leading and trailing parts. The linear polarization is much stronger at low frequencies.

3.9 PSR J1545–4550

Fig. A9 shows the polarization pulse profiles of PSR J1545–4550. At 20 cm, Burgay et al. (2013) shows an component around phase 0.35 that we do not see in our analysis. We have confirmed with the High Time Resolution Universe (HTRU) collaboration that this extra component was caused by an error in their analysis. Our profiles are similar in 10 cm and 20 cm bands. We also show that low-level emission extends over at least 80 per cent of the pulse period. There is evidence of an orthogonal transition between the main pulse and the trailing component.

3.10 PSR J1600–3053

Fig. A10 shows the polarization pulse profiles of PSR J1600–3053. At 20 cm, our results are generally consistent with previously published results (Ord et al. 2004; Yan et al. 2011b), showing orthogonal transitions near the peaks of the two main components. The leading component of the main pulse has flatter spectrum compared with the main component. The central part of the pulse profile depolarizes rapidly with decreasing frequency. We see a sign swap of the circular polarization of the leading component from 20 cm to 10 cm, and at 50 cm, the circular polarization becomes almost zero across the whole profile.

3.11 PSR J1603–7202

Fig. A11 shows the polarization pulse profiles of PSR J1603–7202. At 20 cm, our results are in good agreement with previously published results (Ord et al. 2004; Yan et al. 2011b). The broad low-level feature preceding the main pulse and the double-peak trailing pulse can be clearly identified. We find that there is low-level emission connecting the main pulse and the double-peak trailing pulse, and it becomes stronger at 10 cm. The relative strength of the two main peaks evolves significantly with frequency. As frequency goes down, the second main peak becomes highly circular polarized.

3.12 PSR J1643–1224

Fig. A12 shows the polarization pulse profiles of PSR J1643–1224. At 20 cm, our results are in good agreement with, and extend, previously published results (Ord et al. 2004; Yan et al. 2011b). The PA of the broad feature preceding the main pulse is determined and found to be discontinuous with the rest of the PA variation, showing an orthogonal transition. The main pulse clearly has multiple components and the trailing part has much steeper spectrum than other parts. The leading and trailing parts of the pulse have different apparent RMs.

3.13 PSR J1713+0747

Fig. A13 shows the polarization pulse profiles of PSR J1713+0747. At 20 cm, the S/N of the profile of total intensity is $\sim 10,300$. Our results are consistent with previously published results (Ord et al. 2004; Yan et al. 2011b), showing the almost complete linear polarized leading and trailing components. We detect weak emission around phase ~ -0.2 at 20 cm, which increase the overall width from 104° (as previously thought) to 131° . The non-orthogonal transition preceding the trailing pulse component reported by Yan et al. (2011b) is observed at 10 cm and 50 cm, but at 20 cm MHz the PA transition is continuous. The linear polarization of the leading and trailing components become stronger at low frequencies relative to the rest of the profile. The main peak of the profile clearly has multiple components, and different components have different apparent RMs.

3.14 PSR J1730–2304

Fig. A14 shows the polarization pulse profiles of PSR J1730–2304. At 20 cm, our results are consistent with previously published results (Ord et al. 2004; Yan et al. 2011b). We clearly show the weak leading and trailing components already reported, and detect a weaker leading component not discovered before (around phase ~ 3.2). This increases overall width of the pulse from 232° to 248° . The pulse profile is very complex, with four clear peaks across the main pulse. The central peak at 20 cm band has a steeper spectrum compared with other components. As the frequency goes down, the second peak depolarizes rapidly. The PA variations are very complex and are different in the three bands, leading to apparent RM variations across the profile.

3.15 PSR J1744–1134

Fig. A15 shows the polarization pulse profiles of PSR J1744–1134. At 20 cm, our results are consistent with previously published results (Yan et al. 2011b). The multiple-component precursor is clearly identified and no significant post-cursor component is observed. While the PAs of the main pulse show a smooth decrease, those of the precursor have clear structures and do not simply connect with the rest of the PA variations. The shape of the PA curves are similar in the three bands and the phase-resolved RMs are almost constant. The main pulse is highly linearly polarized from 10 cm to 50 cm. The circular polarization of main pulse grows stronger from 10 cm to 20 cm, but is weaker at 50 cm.

3.16 PSR J1824–2452A

Fig. A16 shows the polarization pulse profiles of PSR J1824–2452A, which is in the globular cluster M28 (Lyne et al. 1987). We used a baseline duty cycle of 0.05 in our processing. At 20 cm, our results are consistent with and extend previously published results (Ord et al. 2004; Yan et al. 2011b). The weak component around phase -0.4 is clearly shown and is highly linearly polarized with a flat spectral index. At 20 cm, we also show that there is low-level bridge emission connecting the two the main components of the pulse profile. The PAs of preceding components are continuous themselves, but are discontinuous with the rest of the PA variations. The frequency evolution of the total intensity is significant and our results are consistent with previous low frequency observations (e.g., Stairs et al. 1999). The phase-resolved spectral indice show huge variations related to the different components.

3.17 PSR J1832–0836

Fig. A17 shows the polarization pulse profiles of PSR J1832–0836. At 20 cm, our results are consistent with, and extend, previously published results (Burgay et al. 2013). The components around phase -0.45 and -0.08 are highly linearly polarized and have relatively flat spectrum. The PAs around phase -0.05 and 0.3 seem to be discontinuous, but is hard to confirm because of the low S/N.

3.18 PSR J1857+0943

Fig. A18 shows the polarization pulse profiles of PSR J1857+0943. At 20 cm, our results are generally consistent with previously published results (Xilouris et al. 1998; Yan et al. 2011b). We show more details of the PA variation, which is very complex and inconsistent with the RVM. At the leading edge of the main pulse, the PA decreases rapidly followed by an orthogonal mode transition. Around phase 0.05 , there is evidence of a non-orthogonal transition. Close to the peak of the interpulse, the PA shows a discontinuity at 20 cm, but becomes continuous at 10 cm. Both the main pulse and the interpulse have multiple components. The profile is largely frequency-dependent and the frequency development we observed is consistent with previous published results (Thorsett & Stinebring 1990). At 50 cm there is a new linear polarization component appearing close to the center of the pulse.

3.19 PSR J1909–3744

Fig. A19 shows the polarization pulse profiles of PSR J1909–3744. At 20 cm, our results are generally consistent with results of Ord et al. (2004); Yan et al. (2011b), showing a narrow main pulse and a weak feature preceding the main pulse by about 0.45 in phase. The frequency evolution of pulse profile is little, however, the fractional linear polarization increases as the frequency decreases.

3.20 PSR J1939+2134

Fig. A20 shows the polarization pulse profiles of PSR J1939+2134. At 20 cm, our results are generally consis-

tent with previously published results (Yan et al. 2011b). As explained in Yan et al. (2011b), because of the high DM/P, our observations are significantly affected by DM smearing, and we do not see the secondary maxima at the trailing edges of both the main pulses and interpulse (Thorsett & Stinebring 1990; Stairs et al. 1999; Ord et al. 2004). We confirm the existence of weak components preceding both the main pulse and interpulse and show that they are highly linear polarized and stronger at 10 cm. Our results show stronger left-circular emission in the main pulse compared to Yan et al. (2011b). The interpulse has steeper spectrum compared with the main pulse, and has a significantly different RM. The fractional linear polarization of the main pulse increases significantly as frequency decreases while that of the interpulse decreases.

3.21 PSR J2124–3358

Fig. A21 shows the polarization pulse profiles of PSR J2124–3358. We used a baseline duty cycle of 0.05 in our processing. At 20 cm, the complex profile we show here is generally consistent with previously published results (Yan et al. 2011b). We are able to provide more details of the PA variation and show that it has complex structures. At 20 cm, around phase 0.03 and −0.5, there are evidences of two orthogonal mode transitions. At 50 cm, around phase 0.1, there is a non-orthogonal transition of $\sim 110^\circ$. Because of the complexity of the profile, profile evolution is hard to describe. There are large variations of spectral index across the pulse longitude and these seem to be related to the different components, but this is complicated by the overlap of different components. We have tested that the phase-resolved spectral index we present here is not significantly affected by the choice of baseline duty cycle and is generally consistent with that of Manchester & Han (2004). The fractional linear polarization of the main pulse increases at lower frequencies.

3.22 PSR J2129–5721

Fig. A22 shows the polarization pulse profiles of PSR J2129–5721. At 20 cm, our results are in good agreement with and extend previously published results (Yan et al. 2011b). The weaker leading shelf of emission extends to at least phase of −0.4, and the post-cursor clearly has multiple components. We show more details of PA in the trailing edge of the main pulse. The PA decreases across the main pulse, and then increases quickly followed by an orthogonal mode transition. The post-cursor of the main pulse has much flatter spectrum. The fractional linear polarization of the main pulse increases as frequency decreases.

3.23 PSR J2145–0750

Fig. A23 shows the polarization pulse profiles of PSR J2145–0750. At 20 cm, our results are in good agreement with and extend previously published results (Yan et al. 2011b). Around phase 0.4, there is evidence of low-level emission which significantly extends the overall width of this MSP from 187° to 277° . The trailing emission and

the weak leading component have steeper spectra compared with other components.

3.24 PSR J2241–5236

Fig. A24 shows the polarization pulse profiles of PSR J2241–5236. At 20 cm, our results generally agree with, and extend, previously published results (Keith et al. 2011). We show a new low-level component around phase 0.4 with a width of ~ 0.2 . We also show more details of the complex PA variations and there is evidence for two orthogonal mode transitions close to the peak. The frequency evolution of pulse profile is hard to see, but the fractional linear polarization increases at lower frequencies.

4 DISCUSSION

4.1 Pulse widths

One of the most fundamental properties of the pulse profile is the pulse width. However, the pulse width is difficult to interpret, particularly for profiles that contain multiple components. Comparing pulse widths across wide frequency bands is even more challenging as the components often differ in spectral index or new components appear in the profile. Traditionally pulse widths are published as the width of the profile at 10 and 50 per cent of the peak flux density (W_{10} and W_{50} respectively). For comparison with previous work, W_{10} and W_{50} are given in Table 3 for the three observing bands of each pulsar. However, these values have limited value. For instance, the W_{10} measurement for PSR J1939+2134 in all three bands provides a measure of the width between the two distinct components. The W_{50} measurement does the same for the 20 cm and the 50 cm observing bands, but in the 10 cm band one of the components does not reach the 50 per cent height of the peak component. The meaning of the W_{50} measurement is therefore different in the 10 cm band.

Following Yan et al. (2011b) we also present the “overall pulse width” for the three bands of each pulsar. This is measured to give the pulse width in which the pulse intensity significantly exceeds the baseline noise (3σ). This value is presented in the first three columns of Table 3. The overall widths have, in most cases, increased from the results published by Yan et al. (2011b) as our higher S/N profiles have allowed us to identify new low-level emission over more of the pulse profile. With the S/N currently achievable (up to $\sim 33,500$ for PSR J0437–4715 20 cm profile) we find that 18 of the 24 pulsars exhibit emission over more than half of the pulse period. Even though the individual pulse components vary with observing frequency, the overall pulse width is relatively constant for pulsars that have high S/N profiles in all three bands. This suggests that, even though the properties of individual components vary across observing bands, the absolute width of the emission beam is more constant.

In terms of pulsar timing, the “sharpness” of the profile provides a measure of how precisely pulse times-of-arrival can be measured. We measure the sharpness of profiles with the effective pulse width defined as

$$W_s = \frac{\Delta\phi}{\sum_i [I(\phi_{i+1}) - I(\phi_i)]^2}, \quad (4)$$

where $\Delta\phi$ is the phase resolution of the pulse profile (measured in units of time), and the profile is normalized to have a maximum intensity of unity (Cordes & Shannon 2010; Shannon et al. 2014). This parameter for each of the observing bands is presented in the last three columns of Table 3.

In some cases it is possible to identify a well-defined pulse component over multiple observing bands. This allows us to investigate the frequency evolution of the component width and separation. Such components have been identified in Fig. A1 to A24 with component numbers (C1 to C28). The width of each component is shown in Table 4. In order to mitigate the effects of surrounding components and low-level features, for each component we provide a measure of its width at 50 and 80 per cent of its peak flux density (W50 and W80 respectively) as a function of observing frequency. We estimated the uncertainties of measurements as the variation of widths when we adjust the 50 and 80 per cent flux density cuts by amount of the baseline rms noise. In most cases the pulse widths decrease with increasing frequency despite of the relatively large uncertainty. However, for PSRs J1939+2134 and J2241–5236, we find an increase of the pulse width with increasing observing frequency. Possible reasons for this are described in Section 5.

The component separations are shown in Table 5. We estimated the uncertainties of measurements as the variation of component separations when we adjust the peak flux density by amount of the baseline rms noise. Within the uncertainty, most cases show no significant frequency evolution of component separations. For PSR J0711–6830, we see an increase of the component separation with decreasing observing frequency, which is likely because of the steep spectrum at the trailing edge of the main pulse.

4.2 Flux Densities and Spectral indices

In Table 6, we present the flux densities and spectral indices for all the MSPs in our sample. As described in Section 2.2, measuring flux densities is not trivial as each pulsar's flux density varies because of diffractive and refractive scintillation. Using summed profiles weighted by $(S/N)^2$ leads to results that are biased high. For the analysis presented here we therefore make use of the individual profiles.

For each individual observation of each pulsar we calculate the mean flux density by averaging over the entire Stokes I profile. The S_{730} , S_{1400} and S_{3100} measurements given in Table 6 are calculated by averaging all the mean flux densities for a given pulsar in an observing band. The variance of the individual measurements in the three bands are tabulated as S_{730}^{RMS} , S_{1400}^{RMS} and S_{3100}^{RMS} respectively. The uncertainty of the mean flux density is estimated as, $S^{\text{RMS}}/(N - 1)^{1/2}$, and N is number of observations. The mean flux densities of several pulsars (e.g., PSRs J0711–6830, J1022+1001) are significantly different to Yan et al. (2011b). For these pulsars we found that they have relatively large flux variances comparable with their mean flux densities, indicating that the flux discrepancies with previous work are caused by interstellar scintillation effects.

The S/N that we obtain in individual observations for most of the pulsars allows us to obtain measurements of the variation in the flux density over each observing band. We therefore divided each band into eight subbands (for

PSRs J1545–4550 and J1832–0836, we only have a few observations in the 50 cm band and the S/N are low, therefore we did not present their flux densities in the 50 cm band). Flux densities are obtained in each subband and are plotted in Fig. 1. The best fit power-law spectra are indicated with red dashed lines and the corresponding spectral indices, α_1 , given in Table 6. For several pulsars (e.g., PSRs J0437–4715, J1022+1001, J2241–5236), the flux density fluctuations caused by interstellar scintillation result in large uncertainties in mean flux densities and affect the fitting for spectral index, especially when the spectrum deviates from a single power-law. Therefore, for comparison, we also calculated flux densities using the summed profiles only weighted by the observing time. The uncertainty of flux density is estimated as the baseline rms noise of the profile. The best fit power-law spectra are indicated with black dashed lines in Fig. 1 and the corresponding spectral indices, α_2 , given in the last column of Table 6.

As shown in Fig. 1, the spectrum of some MSPs can be generally modelled as a single power-law across a wide range of frequency (e.g., PSRs J0613–0200, J0711–6830, J1017–7156, J1643–1224, J1824–2452A, J1939+2134). For most pulsars whose spectra deviate from a single power-law, their spectra become steeper at high frequencies (e.g., PSRs J0437–4715, J1024+0719, J1603–7202) as also reported in normal pulsars (e.g., Maron et al. 2000). Exceptions are PSRs J1022+1001 and J2241–5236 whose spectra become flatter at high frequencies. For PSRs J1600–3053, J1713+0747, J2124–3358, J2145–0750 and J2241–5236, we observed positive spectral indices within the 50 cm band, indicating the existence of spectral turnover at around 1 GHz as have been observed in normal pulsars (e.g., Kijak et al. 2011). For pulsars whose spectra significantly deviate from a single power-law and have large flux density fluctuations, for instance PSRs J1022+1001, J1024–0719 and J2241–5236, the spectral index, α_1 and α_2 , show large differences. For PSRs J1446–4701, J1832–0836 and J2129–5721, the flux densities in the 10 cm band are likely affected by the limited number of observations available and therefore suffered from scintillation effects.

The spectral indices are consistent with the results presented in Toscano et al. (1998), but our measurements have significantly smaller uncertainties. However, compared with Kramer et al. (1999a), the spectral indices do show discrepancies for some pulsars. For instance, we obtained a much steeper spectrum for PSR J0437–4715, which is dominated by the shape of the spectrum in the 10 cm and 20 cm band. The spectrum becomes flatter in the 50 cm band, and therefore the discrepancy is likely because Kramer et al. (1999a) used a very wide frequency range without any information within bands. This indicates that, although the spectra of MSPs could generally follow a single power-law over a wide range of frequency, the spectra could be complex and show different shapes within narrow ranges of frequency. We derived a mean spectral index of -1.76 ± 0.01 for α_1 and -1.81 ± 0.01 for α_2 . This is consistent with previous results of MSPs (Toscano et al. 1998; Kramer et al. 1999a) and close to the observed spectral index of normal pulsars (Lorimer et al. 1995; Maron et al. 2000).

The bottom part of the left-side panels of Fig. A1 to A24 shows the phase-resolved spectral index for each MSP. As the phase-resolved spectral index is derived from

Table 3. Pulse widths for PPTA MSPs.

PSR	Overall width			W_{10}			W_{50}			W_s		
	50 cm (deg)	20 cm (deg)	10 cm (deg)	50 cm (deg)	20 cm (deg)	10 cm (deg)	50 cm (deg)	20 cm (deg)	10 cm (deg)	50 cm (μ s)	20 cm (μ s)	10 cm (μ s)
J0437–4715	321.3	300.2	350.5	130.5	63.4	18.6	15.4	8.9	5.6	127.5	77.3	45.3
J0613–0200	143.0	145.1	126.1	105.9	109.1	105.4	10.5	54.9	30.4	19.7	42.0	49.5
J0711–6830	272.7	284.7	238.9	180.9	168.2	167.8	131.4	124.3	108.7	92.8	74.3	93.6
J1017–7156	46.6	69.2	46.6	22.2	21.7	34.4	16.1	10.7	11.0	28.0	37.2	43.4
J1022+1001	66.9	71.8	61.9	41.9	43.0	35.8	16.5	21.1	8.2	171.3	124.5	171.8
J1024–0719	153.4	271.0	124.6	123.6	109.6	113.7	67.3	35.7	32.0	54.3	66.8	62.9
J1045–4509	53.5	91.6	23.2	70.3	69.7	66.6	33.5	36.6	35.7	328.7	278.3	297.8
J1446–4701	37.3	189.5	49.3	49.3	45.2	37.7	12.4	12.2	11.5	36.7	45.0	39.4
J1545–4550	236.0	250.1	229.7		56.8	43.9		12.8	9.2		55.4	39.1
J1600–3053	55.7	76.8	63.4	48.6	41.3	42.1	11.2	9.3	22.7	70.5	62.5	46.2
J1603–7202	76.4	230.1	222.4	48.3	41.8	38.5	32.4	29.4	7.0	203.8	143.4	147.7
J1643–1224	164.1	221.9	192.3	83.8	72.6	65.7	32.8	24.9	20.5	245.2	209.1	159.7
J1713+0747	98.9	198.5	99.6	42.3	30.3	29.6	16.4	8.8	8.3	120.4	64.6	58.6
J1730–2304	188.3	252.3	198.5	68.9	76.0	73.0	34.2	43.2	43.8	164.9	99.1	90.2
J1744–1134	167.9	200.6	160.8	24.0	21.9	20.1	13.1	12.3	8.8	65.2	64.8	57.1
J1824–2452A	288.0	283.8	190.6	219.1	191.0	170.0	113.4	115.4	7.7	47.2	30.1	40.9
J1832–0836	124.0	285.3	253.6		244.1	213.7		113.2	6.9		13.5	22.9
J1857+0943	223.8	242.5	232.6	219.0	202.4	203.4	42.4	35.2	31.2	101.2	106.7	59.4
J1909–3744	178.2	190.2	19.0	13.1	11.0	9.2	6.9	5.3	4.3	27.7	22.8	19.4
J1939+2134	306.4	337.4	306.4	207.0	199.3	204.5	195.1	182.1	10.5	16.3	25.0	21.5
J2124–3358	320.6	332.2	281.2	255.1	269.7	282.9	168.3	37.5	31.8	96.2	153.4	121.9
J2129–5721	72.6	157.8	67.6	37.5	60.0	88.4	22.9	25.5	53.8	74.7	78.8	50.9
J2145–0750	256.5	267.4	180.9	94.1	93.6	91.1	9.1	7.6	7.8	206.8	206.6	196.0
J2241–5236	74.7	209.9	43.7	18.8	20.3	21.0	10.3	10.6	9.8	26.3	28.7	26.8

Table 4. Widths of pulse components for PPTA MSPs whose mean pulse profiles have multiple, well defined components.

PSR	Component	W_{50}			W_{80}		
		50 cm (deg)	20 cm (deg)	10 cm (deg)	50 cm (deg)	20 cm (deg)	10 cm (deg)
J0711–6830	C1	15 ± 4	10 ± 1	8.8 ± 0.7	5.6 ± 0.7	5.3 ± 0.7	4.2 ± 0.7
J1017–7156	C3	16 ± 1	10 ± 3	10 ± 1	9 ± 3	6 ± 3	6 ± 3
J1600–3053	C9	11 ± 1	9.2 ± 0.7	7 ± 3	6 ± 1	5 ± 1	3 ± 1
J1603–7202	C10	12.7 ± 0.7	7.4 ± 0.7	7.0 ± 0.7	6.7 ± 0.7	3.9 ± 0.7	3.9 ± 0.4
	C11	14.1 ± 0.7	11.3 ± 0.7	9.9 ± 0.7	7.4 ± 0.4	6.3 ± 0.7	5 ± 2
J1643–1224	C12	33 ± 1	25 ± 1	20 ± 1	17 ± 1	11 ± 1	8 ± 1
J1713+0747	C13	17 ± 1	8.8 ± 0.7	8 ± 2	6.3 ± 0.7	4.2 ± 0.7	3.9 ± 0.7
J1744–1134	C16	13.0 ± 0.7	12.3 ± 0.7	8.8 ± 0.7	7 ± 1	4.9 ± 0.7	3.9 ± 0.7
J1824–2452A	C18	13 ± 3	9 ± 3	9 ± 3	7 ± 3	4 ± 3	6 ± 2
J1909–3744	C21	6 ± 1	5 ± 1	4 ± 1	2 ± 1	2 ± 1	2 ± 1
J1939+2134	C22	11 ± 3	14 ± 3	11 ± 3	7 ± 3	9 ± 3	7 ± 3
	C23	13 ± 3	16 ± 3	11 ± 3	7 ± 3	9 ± 3	6 ± 3
J2145–0750	C26	8.8 ± 0.7	7.7 ± 0.7	8.1 ± 0.7	4.6 ± 0.7	3.5 ± 0.7	3.2 ± 0.7
J2241–5236	C28	11 ± 1	11 ± 1	10 ± 1	4 ± 1	6 ± 1	6 ± 1

the summed profiles weighted by the observing time, we compare them with the mean spectral index, α_2 , which is shown with a red dashed line in each figure and its uncertainty shown as yellow highlighted region. In many cases the spectral indices vary significantly at different profile phases. For instance, in PSR J0437–4715 the spectral index varies from ~ -1 to ~ -2 in different parts of the profile.

For PSR J1022+1002 one component has a spectral index ~ -1.5 and the other ~ -2.5 .

In most, but not all, cases the variations in the spectral index as a function of phase follow the components in the total intensity profile. Although we do not find strong correlations between the phase-resolved spectral index and the pulse profile, we clearly see that different pulse profile

Table 5. Component separation for PPTA MSPs whose mean pulse profile have multiple, well defined components.

PSR	Component	Component separation		
		730 MHz (deg)	1400 MHz (deg)	3100 MHz (deg)
J0711–6830	C1, C2	99.6 ± 0.6	97.1 ± 0.4	91.1 ± 0.6
J1022+1001	C4, C5	12.0 ± 0.4	12.0 ± 0.5	12.0 ± 0.5
J1024–0719	C6, C7	16.2 ± 0.5	16.5 ± 0.4	17.6 ± 0.3
J1600–3053	C8, C9	9 ± 3	12.0 ± 0.8	14 ± 1
J1603–7202	C10, C11	21.1 ± 0.7	21.8 ± 0.5	21.8 ± 0.9
J1730–2304	C14, C15	17.9 ± 0.4	17.2 ± 0.5	12.7 ± 0.5
J1824–2452A	C17, C18	106 ± 2	107 ± 2	110 ± 2
J1857+0943	C19, C20	165.4 ± 0.6	164.0 ± 0.4	163.3 ± 0.7
J1939+2134	C22, C23	172 ± 2	174 ± 2	172 ± 2
J2129–5721	C24, C25	10.6 ± 0.8	11 ± 1	8 ± 3
J2145–0750	C26, C27	78.1 ± 0.4	79.2 ± 0.4	79.5 ± 0.8

components usually have different spectral indices. In some cases, the peaks of pulse profile components coincide with the local maximum or minimum of the phase-resolved spectral index.

The uncertainties placed on the phase-resolved spectral indices are determined from the errors in determining the flux density in the different observing bands and also from the goodness-of-fit for the single power-law model. Regions with high uncertainties, but high S/N profiles are therefore regions in which the spectra can not be well fitted with a single power-law. Fig. 2 shows the flux density spectra for PSR J1713+0747 at several different pulse phases. Close to phase zero, the turnover of the spectrum at around 1400 MHz becomes significant and therefore the uncertainty of the phase-resolved spectral index is much larger than those at other pulse phases. For almost all pulsars in our sample, the uncertainty of the phase-resolved spectral index varies across the profile, indicating that different profile components can have quite different spectral shapes. For some pulsars (e.g., PSRs J0613–0200, J1643–1224 and J1939+2134), even though their mean flux density follows a single power-law very well across bands, the spectrum of individual profile components significantly deviate from a single power-law.

4.3 Polarization properties

In Table 7, the fractional linear polarization $\langle L \rangle / S$, the fractional net circular polarization $\langle V \rangle / S$ and the fractional absolute circular polarization $\langle |V| \rangle / S$ at different frequencies are presented. The means are taken across the pulse profile where the total intensity exceeds three times of the baseline rms noise. All the polarization parameters are calculated from the average polarization profiles and the uncertainties are estimated using the baseline rms noise. The bottom part of the right-side panels of Fig. A1 to A24 shows the phase-resolved fractional linear polarization for each MSP.

For nine pulsars, we see a clear decrease of the mean fractional linear polarization with increasing frequency. In contrast, for PSRs J1045–4509, J1603–7202 and J1730–2304 and J1824–2452A, the mean fractional linear polarization significantly increases with frequency. Different profile components of a pulsar can show different frequency evolution of the fractional linear polarization. For instance,

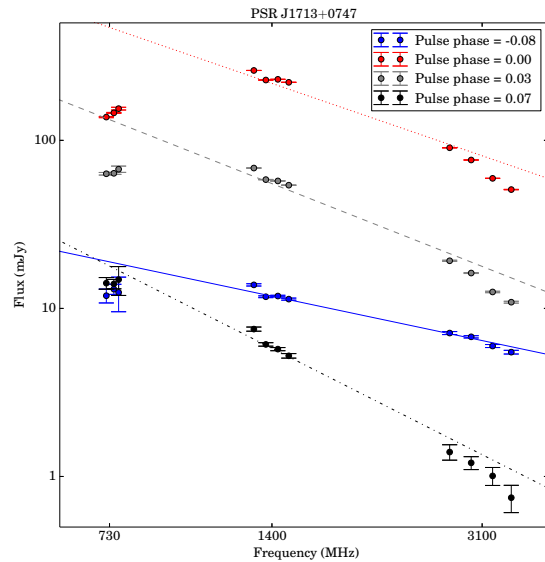


Figure 2. Flux density spectra for PSR J1713+0747 at different pulse phases.

PSR J1643–1224, the fractional linear polarization of the leading edge of the main pulse increases with decreasing frequency while that of the trailing edge decreases with decreasing frequency. There is no evidence that sources that are highly polarized depolarize rapidly with increasing frequency as reported previously (Kramer et al. 1999a).

For most of our MSPs, the phase-resolved fractional linear polarization is remarkably similar at different observing bands (examples include PSR J0437–4715 and J1857+0943). However, for a few pulsars (such as PSR J1022+1001) the fractional linear polarization differs between bands. We find no correlation between the phase-resolved spectral index and the fractional linear polarization. In pulsars such as PSRs J1603–7202, J1939+2134, J2145–0750 and J2241–5236 we see evidence that the main component has a lower fractional linear polarization than leading or trailing components. However, for PSR J1744–1134, we do not see high fractional linear polarizations in the precursor pulse.

Table 6. Flux densities and spectral indices for PPTA MSPs.

PSR	S_{730} (mJy)	S_{730}^{RMS} (mJy)	S_{1400} (mJy)	S_{1400}^{RMS} (mJy)	S_{3100} (mJy)	S_{3100}^{RMS} (mJy)	Spectral index	
							α_1	α_2
J0437–4715	364.3 ± 19.2	255.2	150.2 ± 1.6	42.2	35.6 ± 1.2	20.5	-1.69 ± 0.03	-1.65 ± 0.02
J0613–0200	6.7 ± 0.3	2.3	2.25 ± 0.03	0.4	0.45 ± 0.01	0.1	-1.90 ± 0.03	-1.83 ± 0.03
J0711–6830	11.4 ± 1.0	8.5	3.7 ± 0.4	5.7	0.72 ± 0.04	0.4	-1.94 ± 0.03	-1.83 ± 0.05
J1017–7156	2.5 ± 0.1	0.8	0.99 ± 0.04	0.4	0.21 ± 0.01	0.1	-1.67 ± 0.04	-1.64 ± 0.04
J1022+1001	14.2 ± 2.8	22.9	4.9 ± 0.4	4.6	1.18 ± 0.03	0.4	-1.66 ± 0.03	-1.91 ± 0.06
J1024–0719	5.6 ± 0.8	4.9	2.3 ± 0.2	1.7	0.52 ± 0.01	0.1	-1.80 ± 0.03	-1.62 ± 0.05
J1045–4509	9.2 ± 0.2	1.8	2.74 ± 0.04	0.5	0.48 ± 0.01	0.1	-2.06 ± 0.02	-2.04 ± 0.03
J1446–4701	1.8 ± 0.1	0.5	0.46 ± 0.02	0.2	0.15 ± 0.02	0.07	-2.05 ± 0.07	-1.93 ± 0.09
J1545–4550			0.87 ± 0.05	0.2	0.34 ± 0.04	0.1	-1.15 ± 0.07	-1.13 ± 0.06
J1600–3053	2.9 ± 0.1	0.4	2.44 ± 0.04	0.4	0.84 ± 0.02	0.2	-0.83 ± 0.07	-1.19 ± 0.05
J1603–7202	10.9 ± 0.7	4.9	3.5 ± 0.2	1.7	0.55 ± 0.06	0.4	-2.15 ± 0.06	-2.03 ± 0.05
J1643–1224	12.4 ± 0.2	1.4	4.68 ± 0.06	0.7	1.18 ± 0.02	0.2	-1.64 ± 0.01	-1.66 ± 0.02
J1713+0747	10.1 ± 0.8	6.2	9.1 ± 0.7	8.4	2.6 ± 0.2	1.6	-1.06 ± 0.07	-1.2 ± 0.1
J1730–2304	11.5 ± 0.5	3.9	4.0 ± 0.2	2.0	1.7 ± 0.2	1.5	-1.46 ± 0.06	-1.22 ± 0.07
J1744–1134	8.0 ± 0.7	5.7	3.2 ± 0.3	3.2	0.77 ± 0.05	0.5	-1.63 ± 0.03	-1.58 ± 0.05
J1824–2452A	11.4 ± 0.5	2.9	2.30 ± 0.05	0.4	0.39 ± 0.01	0.1	-2.28 ± 0.03	-2.35 ± 0.03
J1832–0836			1.18 ± 0.07	0.3	0.32 ± 0.03	0.1	-1.66 ± 0.06	-1.60 ± 0.07
J1857+0943	10.4 ± 0.4	3.0	5.1 ± 0.3	2.9	1.2 ± 0.1	0.9	-1.46 ± 0.04	-1.63 ± 0.07
J1909–3744	4.9 ± 0.3	3.1	2.5 ± 0.2	3.2	0.76 ± 0.04	0.5	-1.29 ± 0.02	-1.29 ± 0.03
J1939+2134	67.8 ± 2.7	20.9	15.2 ± 0.6	6.2	1.82 ± 0.09	0.9	-2.52 ± 0.02	-2.54 ± 0.02
J2124–3358	19.3 ± 2.7	17.2	4.5 ± 0.2	2.2	0.82 ± 0.01	0.1	-2.15 ± 0.03	-2.25 ± 0.03
J2129–5721	5.9 ± 0.5	3.9	1.28 ± 0.09	1.0	0.34 ± 0.05	0.2	-2.12 ± 0.07	-2.52 ± 0.05
J2145–0750	27.4 ± 3.4	28.5	10.3 ± 1.0	11.2	1.75 ± 0.07	0.8	-1.98 ± 0.03	-1.94 ± 0.04
J2241–5236	11.9 ± 1.8	16.2	1.95 ± 0.09	1.2	0.35 ± 0.01	0.1	-2.12 ± 0.04	-2.93 ± 0.07

At phase ranges where a PA transition occurs, the fractional linear polarization is significantly lower than other phase ranges, which can be explained as the overlap of orthogonal modes. However, we do not see significantly lower or higher fractional net circular polarization close to PA transitions. We do not find strong relations between the size of the PA transition and the fractional linear polarization. Orthogonal mode transitions normally correspond to lower fractional linear polarization, but we also see low fractional linear polarizations for non-orthogonal transitions, for instance in PSRs J1045–4509 and J1730–2304.

In Fig. 3, the distribution of phase-resolved fractional linear, circular and net circular polarization for 24 MSPs in three bands are shown. To obtain the phase-resolved values, we rebinned the profile in each band into 128 phase bins and only phase bins whose linear or circular polarization exceeds three times of their baseline rms noise were used. While the distributions of the fractional linear polarization are similar across three bands, we see that both the distribution of fractional circular and net circular polarization becomes narrower at lower frequencies. This indicates that the fractional circular and net circular polarization decrease as decreasing frequency.

4.4 Rotation measures

With the aligned, three-band profiles, we can not only determine new rotation measure (RM) values, but also investigate whether the polarization PAs obey the expected λ^2 law. To gain enough S/N, we usually only split the 10 cm and 20 cm band into four subbands and the 50 cm band into three

subbands. For PSR J0613–0200, the linear polarization is weak, and we averaged the entire 10 cm band in frequency and split the 50 cm band into only two subbands. For PSRs J1446–4701, the linear polarization is weak in the 10 cm band and the S/N is low in the 50 cm band, therefore we did not use the 10 cm band and averaged the entire 50 cm band in frequency. For J1545–4550, the S/N of profiles in the 50 cm is very low, therefore we did not use the 50 cm band. For PSR J1832–0836, the S/N of profile is low and the linear polarization is weak in both 10 and 50 cm bands, therefore we excluded it from our RM measurements. For PSR J1857+0934, the linear polarization is weak and the S/N in the 50 cm band is low, and we split the 50 cm band into only two subbands. For PSR J2129–5721, the S/N of 10 cm profile is low and therefore we averaged the entire 10 cm band in frequency.

As the PAs vary significantly with pulse phase and also with observing frequency, we have selected small regions in phase in which the PAs are generally stable across the three bands. Only phase bins whose linear polarization exceeds five times of the baseline rms noise were used in order to avoid bias in calculations of the PAs.

Our results are summarised in Table 8. Previously published results, obtained from the 20 cm band alone, are shown in the second column. In columns 3, 4 and 5 we present our results determined across two bands (10–20, 10–50 and 20–50 respectively). In column 6 we present the RM value obtained by fitting across all three bands. In Fig. 4, the mean PAs in the stable regions for each pulsar, are plotted a function of λ^2 . The best fitted RMs are indicated with red dashed lines.

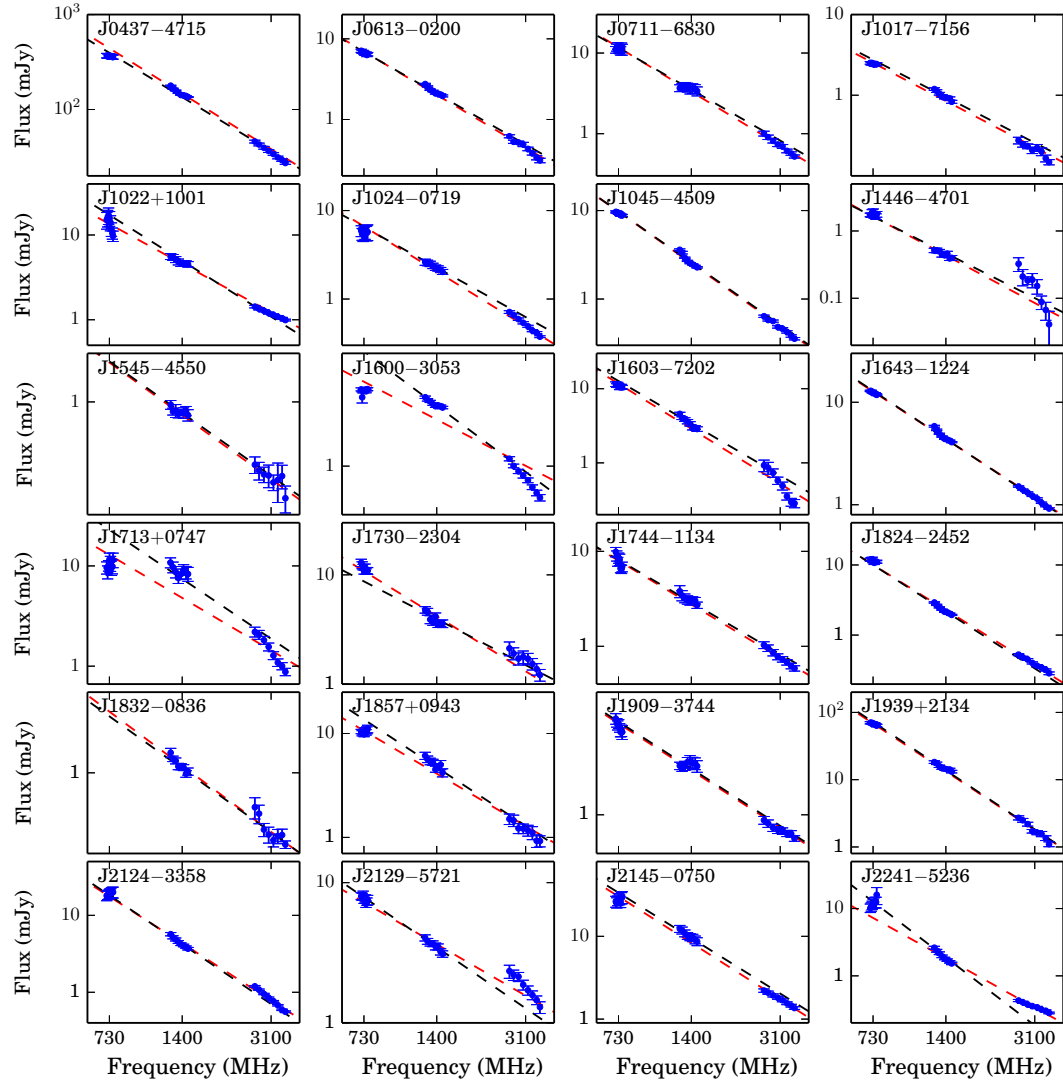


Figure 1. Flux density spectra for 24 MSPs. Red and black dashed lines show the power-law spectra with spectral index α_1 and α_2 respectively.

For some pulsars, our RMs are significantly different from previously published results. These are explained as follows. First, previous measurements were obtained using only the 20 cm band. In Fig. 4 it is clear that for pulsars such as J0437-4715, J1022+1001 and J1744-1134, the PAs in the 20 cm band deviate from the best fitted lines obtained using the wider band. Second, previous measurements used PAs averaged over the pulse longitude while we only averaged PAs within phase ranges that PAs are stable. Therefore, the variation of RM across the pulse longitude would introduce deviations.

Fig. 4 shows that, for some pulsars, the PAs generally obey the λ^2 fit across a wide range of frequency (e.g., PSRs J0613-0200, J0711-6830, J1045-4509, J1643-1224, J1824-2452A). However, for other pulsars, the PAs can significantly deviate from the λ^2 fit across bands (e.g., PSRs J1017-7156, J1713+0747) and show different trends within bands (e.g., PSRs J0437-4715, J1022+1001, J1730-2304,

J1744-1134, J1909-3744, J2124-3358, J2145-0750). For PSRs J2124-3358 and J2129-5721, the deviation of PA in the 10 cm band from the best fitted result is likely caused by the low S/N of the profile. For PSRs J1603-7202 and J2145-0750, the PA curves vary dramatically across bands and cause the deviation of PAs from the λ^2 fit.

The bottom part of the right-side panels of Fig. A1 to A24 shows measurements of RM measured at specific phases for each MSP. Since only phase bins whose linear polarization exceeds five times of the baseline rms noise were used, and we only plot RMs whose uncertainty is smaller than 3 rad m^{-2} , the phase-resolved RMs only cover pulse phases where the linear polarization is strong and PAs generally obey the λ^2 fit. For most pulsars, we can see systematic RM variations across the pulse longitude following the structure of the mean profile. For instance, in PSR J0437-4715 the RM shows complex variations from $\sim -8 \text{ rad m}^{-2}$ to $\sim 8 \text{ rad m}^{-2}$. For PSR J1643-1224, one linear polariza-

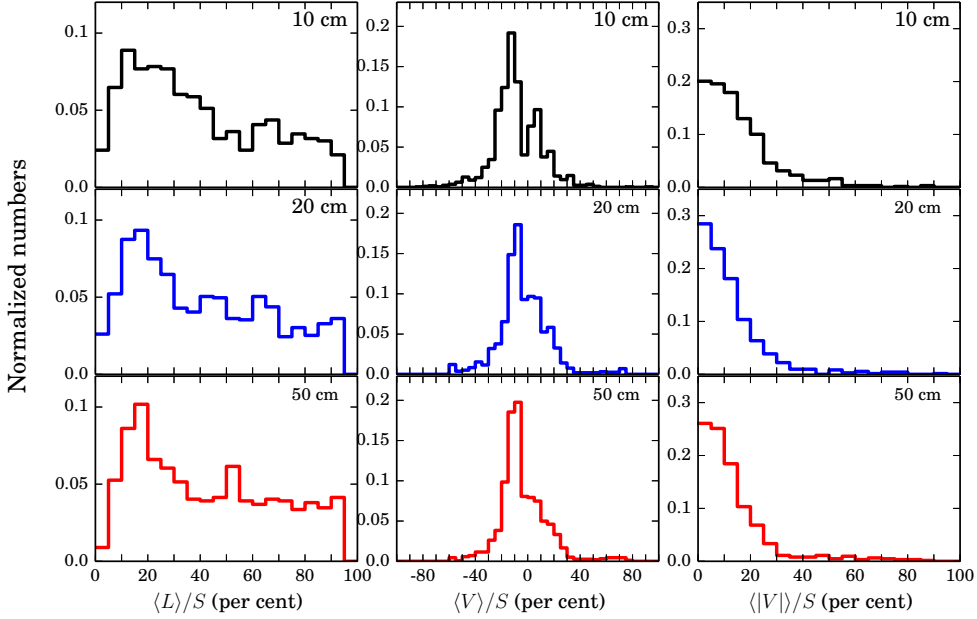


Figure 3. Histograms of the fractional linear, circular and net circular polarization for 24 MSPs in three bands.

Table 7. Polarization parameters for PPTA MSPs.

PSR	$\langle L \rangle / S$			$\langle V \rangle / S$			$\langle V \rangle / S$		
	50 cm (per cent)	20 cm (per cent)	10 cm (per cent)	50 cm (per cent)	20 cm (per cent)	10 cm (per cent)	50 cm (per cent)	20 cm (per cent)	10 cm (per cent)
J0437-4715	26.6 ± 0.0	25.1 ± 0.0	20.4 ± 0.0	-4.2 ± 0.0	-2.9 ± 0.0	-8.0 ± 0.0	15.4 ± 0.0	11.3 ± 0.0	12.4 ± 0.0
J0613-0200	28.9 ± 0.3	21.0 ± 0.1	14.7 ± 0.5	-6.5 ± 0.3	5.2 ± 0.1	10.7 ± 0.6	8.9 ± 0.3	5.6 ± 0.1	11.2 ± 0.6
J0711-6830	24.6 ± 0.2	14.1 ± 0.1	17 ± 2	-12.7 ± 0.2	-12.9 ± 0.1	-24 ± 2	12.7 ± 0.2	13.1 ± 0.1	24 ± 2
J1017-7156	44.5 ± 0.7	35.4 ± 0.3	42 ± 1	6.9 ± 0.8	-28.9 ± 0.2	-38 ± 2	18.5 ± 0.8	29.5 ± 0.2	42 ± 2
J1022+1001	67.9 ± 0.1	56.3 ± 0.0	23.5 ± 0.2	-13.4 ± 0.1	-11.6 ± 0.0	-2.7 ± 0.2	13.4 ± 0.1	12.6 ± 0.0	5.6 ± 0.2
J1024-0719	69.0 ± 0.6	67.9 ± 0.1	61.7 ± 0.8	1.1 ± 0.6	5.5 ± 0.2	6.1 ± 0.7	3.7 ± 0.6	6.3 ± 0.2	6.7 ± 0.7
J1045-4509	18.7 ± 0.3	22.5 ± 0.1	30.2 ± 0.5	8.2 ± 0.3	14.7 ± 0.1	16.4 ± 0.6	10.6 ± 0.3	16.6 ± 0.1	16.5 ± 0.6
J1446-4701	60.4 ± 2.8	38 ± 1		-13 ± 2	-9 ± 1		15 ± 3	11 ± 1	
J1545-4550	61.4 ± 6.6	58 ± 1	59 ± 2	-11 ± 6	-13.2 ± 0.9	-10 ± 2	23 ± 6	17.1 ± 0.9	11 ± 2
J1600-3053	33 ± 2	31.3 ± 0.1	36.8 ± 0.3	0.4 ± 2	3.8 ± 0.1	-2.3 ± 0.3	3 ± 2	4.0 ± 0.1	4.7 ± 0.3
J1603-7202	16.6 ± 0.2	18.6 ± 0.1	31.6 ± 0.7	33.6 ± 0.3	29.0 ± 0.1	15.3 ± 0.8	34.2 ± 0.3	32.4 ± 0.1	22.3 ± 0.8
J1643-1224	20.0 ± 0.3	17.4 ± 0.1	19.9 ± 0.2	6.8 ± 0.2	0.4 ± 0.1	-6.6 ± 0.2	13.9 ± 0.2	13.8 ± 0.1	10.4 ± 0.2
J1713+0747	33.3 ± 0.3	31.5 ± 0.0	27.0 ± 0.1	-2.8 ± 0.2	1.1 ± 0.0	-1.1 ± 0.1	3.9 ± 0.2	3.8 ± 0.0	3.8 ± 0.1
J1730-2304	26.2 ± 0.3	29.2 ± 0.1	44.9 ± 0.2	-19.1 ± 0.3	-19.4 ± 0.1	-11.9 ± 0.2	19.2 ± 0.3	20.6 ± 0.1	15.9 ± 0.2
J1744-1134	88.9 ± 0.4	91.8 ± 0.1	88.0 ± 0.4	0.2 ± 0.4	2.9 ± 0.1	1.5 ± 0.3	0.7 ± 0.4	2.9 ± 0.1	1.6 ± 0.3
J1824-2452A	70.9 ± 0.5	77.8 ± 0.2	84.2 ± 1.0	0.1 ± 0.3	3.5 ± 0.2	-0.8 ± 0.8	3.8 ± 0.3	4.4 ± 0.2	5.5 ± 0.8
J1832-0836		36 ± 2	43 ± 11		3 ± 1	-4 ± 10		10 ± 1	11 ± 10
J1857+0943	20.9 ± 0.9	14.5 ± 0.1	14.1 ± 0.4	-1.2 ± 0.7	2.5 ± 0.1	0.3 ± 0.4	4.7 ± 0.7	5.8 ± 0.1	7.3 ± 0.4
J1909-3744	61.2 ± 0.4	48.7 ± 0.1	26.3 ± 0.2	13.1 ± 0.4	14.9 ± 0.1	5.0 ± 0.2	15.4 ± 0.4	16.1 ± 0.1	6.6 ± 0.2
J1939+2134	38.1 ± 0.1	30.0 ± 0.0	24.3 ± 0.2	0.9 ± 0.1	3.3 ± 0.0	-0.2 ± 0.2	1.1 ± 0.1	3.3 ± 0.0	1.2 ± 0.2
J2124-3358	46.2 ± 0.2	33.1 ± 0.1	49 ± 1	-2.5 ± 0.2	0.4 ± 0.1	-3.9 ± 1.0	3.8 ± 0.2	5.5 ± 0.1	7 ± 1
J2129-5721	66.8 ± 0.6	47.3 ± 0.2	39 ± 8	-27.0 ± 0.6	-24.8 ± 0.2	-16 ± 8	35.5 ± 0.6	26.6 ± 0.2	17 ± 8
J2145-0750	19.2 ± 0.1	15.9 ± 0.0	10.9 ± 0.1	5.9 ± 0.1	9.2 ± 0.0	0.9 ± 0.1	9.5 ± 0.1	10.0 ± 0.0	8.1 ± 0.1
J2241-5236	20.0 ± 0.2	12.6 ± 0.1	12.5 ± 0.7	-2.9 ± 0.2	-0.7 ± 0.1	-4.2 ± 0.7	4.7 ± 0.2	6.2 ± 0.1	8.9 ± 0.7

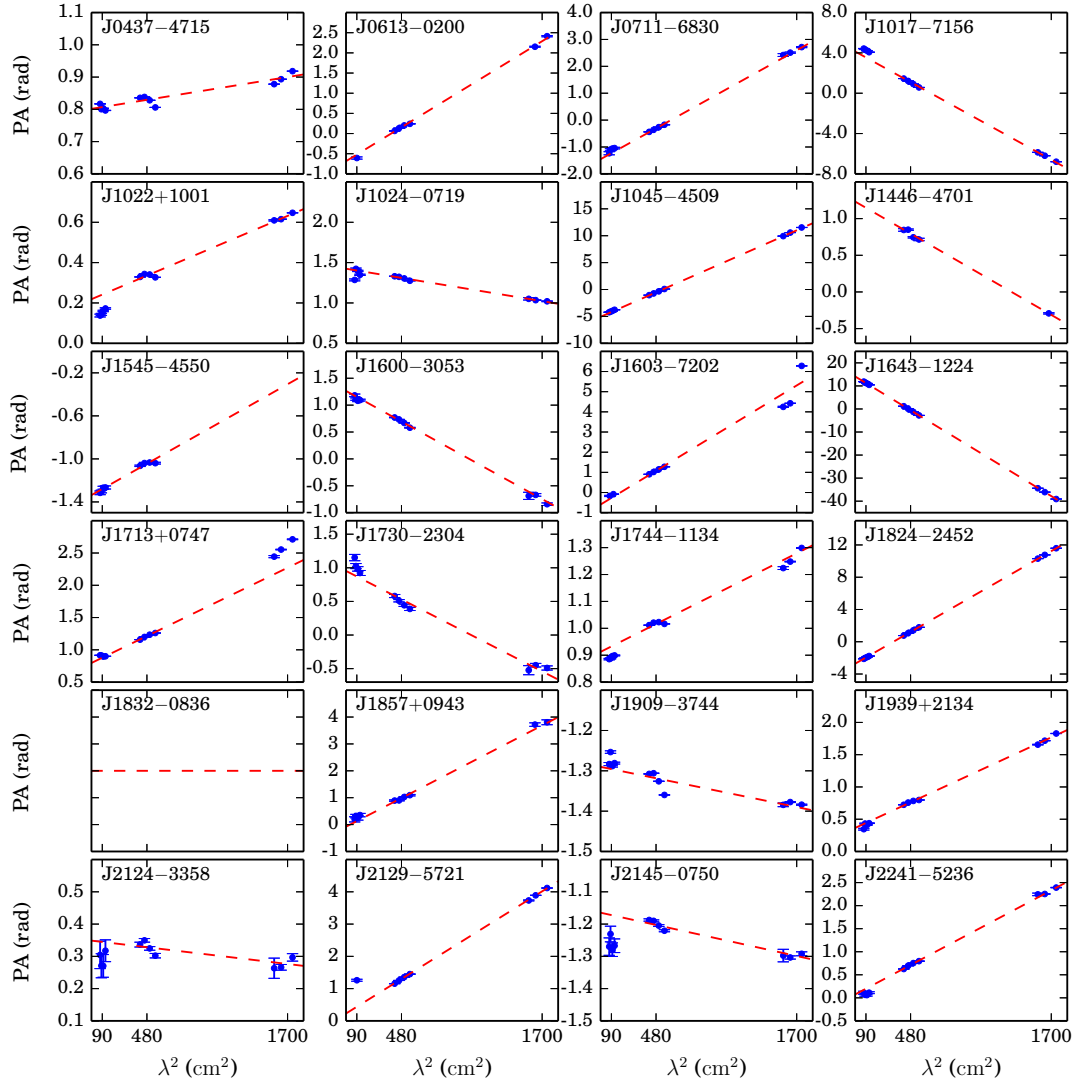


Figure 4. Position angles as a function of λ^2 for 23 MSPs. The fitted RMs are indicated with red dashed lines

tion component has a RM $\sim -306 \text{ rad m}^{-2}$ and the other $\sim -300 \text{ rad m}^{-2}$. We find that significant variations of RM always associate with orthogonal or non-orthogonal mode transitions in PA (e.g., PSRs J1022+1001, J1600-3053, J1643-1224, J1713+0747). For PSR J1744-1134, whose PA curve is smooth across the main pulse, the RMs show minor variations. This is consistent with previous phase-resolved RM study of normal pulsars which also show that the greatest RM fluctuations seem coincident with the steepest gradients of the PA curve, whereas pulsars with flat PA curve show little RM variation (Noutsos et al. 2009).

5 SUMMARY OF RESULTS AND CONCLUSIONS

Our results indicate that:

- Millisecond pulsar profiles are complex and wide. This

is not a surprise and has been presented in numerous earlier publications. We have shown that 18 of the 24 MSPs exhibit emission over more than half of the pulse period and the overall pulse width is relatively constant for pulsars that have high S/N profiles in all three bands. The MSPs in our sample do not show the frequency evolution of the component separations (Kramer et al. 1999a) that has been observed in normal pulsars (e.g., Cordes 1978; Thorsett 1991). This supports the idea that the MSP radio emission is emitted from the outer magnetosphere (Manchester et al. 2005; Ravi et al. 2010) and that caustic effects may account for the broad frequency-independent pulse profiles (Dyks & Rudak 2003; Watters et al. 2009).

- The spectrum of some of the pulsars in our sample significantly deviates from a single power-law across the different observing bands. We have observed the spectral shape steepening at high frequencies and, for some pulsars, there is possible evidence of a spectral turnover at around 1 GHz. Similar features have been identified in normal pul-

Table 8. Interstellar RMs for 23 MSPs in units of rad m⁻². Previously published results without footnotes are from Yan et al. (2011b).

PSR	Previously published		Measured from mean profile		
	20 cm	10cm - 20cm	10cm - 50cm	20cm - 50cm	fitting
J0437–4715	0.0 ± 0.4	0.60± 0.01	0.618± 0.004	0.624± 0.001	0.58± 0.09
J0613–0200	9.7 ± 1.1	19.8± 0.7	17.8± 0.2	17.20± 0.08	17.5± 0.3
J0711–6830	21.6 ± 3.1	22.1± 0.4	23.5± 0.1	23.89± 0.05	23.9± 0.4
J1017–7156	−78 ± 3 ^a	−82.1± 0.2	−66.59± 0.04	−61.66± 0.03	−63± 1
J1022+1001	−0.6 ± 0.5	4.68± 0.06	2.95± 0.01	2.405± 0.004	2.4± 0.1
J1024–0719	−8.2 ± 0.8	−1.88± 0.09	−2.26± 0.03	−2.38± 0.02	−2.4± 0.2
J1045–4509	92.0 ± 1.0	91.5± 0.1	93.34± 0.06	93.91± 0.07	94.7± 0.7
J1446–4701	−14 ± 3 ^a			−8.98± 0.11	−9.1± 0.2
J1545–4550	−0.6 ± 1.3 ^b	6.3± 0.2	4.1± 0.2	3.4± 0.2	6.1± 0.5
J1600–3053	−15.5 ± 1.0	−11.6± 0.1	−11.77± 0.09	−11.8± 0.1	−11.8± 0.3
J1603–7202	27.7 ± 0.8	31.2± 0.4	28.91± 0.09	28.20± 0.05	35± 2
J1643–1224	−308.1 ± 1.0	−306.8± 0.2	−301.70± 0.06	−300.09± 0.05	−305.7± 0.2
J1713+0747	8.4 ± 0.6	8.19± 0.02	10.67± 0.02	11.45± 0.03	8.7± 0.5
J1730–2304	−7.2 ± 2.2	−13.4± 0.2	−9.22± 0.08	−7.88± 0.1	−8.8± 0.6
J1744–1134	−1.6 ± 0.7	3.24± 0.02	2.34± 0.01	2.05± 0.01	2.2± 0.2
J1824–2452A	77.8 ± 0.6	82.6± 0.3	82.06± 0.07	81.91± 0.04	82.2± 0.2
J1857+0943	16.4 ± 3.5	18.4± 0.8	21.4± 0.3	22.4± 0.3	22.2± 0.9
J1909–3744	−6.6 ± 0.8	−0.38± 0.02	−0.30± 0.01	−0.27± 0.01	−0.6± 0.2
J1939+2134	6.7 ± 0.6	12.3± 0.2	9.13± 0.05	8.11± 0.01	8.3± 0.1
J2124–3358	−5.0 ± 0.9	1.6± 0.3	0.07± 0.08	−0.41± 0.03	−0.4± 0.1
J2129–5721	23.5 ± 0.8	0.00± 0.06	16.61± 0.02	21.88± 0.03	22.3± 0.3
J2145–0750	−1.3 ± 0.7	1.4± 0.3	−0.31± 0.09	−0.85± 0.04	−0.8± 0.1
J2241–5236	14 ± 6 ^c	16.1± 0.3	13.84± 0.08	13.14± 0.04	13.3± 0.1

^a Keith et al. (2012); ^b Burgay et al. (2013); ^c Keith et al. (2011).

sars (e.g., Maron et al. 2000; Kijak et al. 2011). However, previous measurements of MSP flux densities over a wide frequency range did not show such phenomena (Kramer et al. 1999a; Kuzmin & Losovsky 2001). This is likely because, in contrast to earlier work, we have measured multiple flux density values within each observing band.

We have also observed the spectral shape flattening within bands at high frequencies for PSRs J1022+1001 and J2241–5236. Such flattening or turn-up of the spectrum has only been previously observed at extremely high frequencies (~ 30 GHz) (Kramer et al. 1996), and has been explained by refraction effects (Petrova 2002). However, the spectral flattening that we have observed is more likely to be local spectral features and we would expect the power-law shape, in general, to continue over much wider bands.

- For almost all of the MSPs in our sample, the observed three-band PA variations across the profile are extremely complicated and cannot be fitted with using the RVM. We show complex details of the PA variation for several MSPs, which were previously thought to have relatively flat or smooth PA profiles (e.g., PSRs J1024–0719, J1600–3053, J1744–1134, J2124–3358). Across bands, the PA profiles can evolve significantly (e.g., PSRs J0437–4715, J0711–6830, J1603–7202, J1730–2304).

One exception is PSR J1022+1001, whose PA profile is relatively smooth in all three bands except for a discontinuity close to phase zero. At 10 cm, the PA variation fits the RVM very well. The PA variation departs from the RVM progressively with decreasing frequency. One model to explain this would be that at higher frequencies and lower emission heights, the magnetic field is closer to a simple

dipolar field. As the frequency decreases, the magnetic field departs from this simple dipolar form.

- We have observed systematic variations of apparent RM across the pulse longitude following the structure of the mean profile, indicating that such variations are likely to arise from the pulsar magnetosphere. We have also shown that the PA of some pulsars does not follow the χ^2 fit. As discussed in Noutsos et al. (2009), possible explanations of these phenomena includes Faraday rotation in the pulsar magnetosphere (Kennett & Melrose 1998; Wang et al. 2011), the superposition and frequency dependence of quasi-orthogonal polarization modes (Ramachandran et al. 2004) and interstellar scattering (Karastergiou 2009).

- Different pulse components usually have differing spectral indices, apparent RMs and fractional polarizations. Measurements of flux density as a function of frequency for individual components can significantly differ from that obtained by averaging over the entire profile. The spectral shape also often deviates from a single power-law. The fractional polarization increases with increasing frequency for some components, but decreases for other components. These results suggest that there are multiple emission regions or structures within the pulsar magnetosphere and that pulse components originate in different locations within the magnetosphere (e.g., Dyks et al. 2010).

The main goal of this paper has been to inspire and promote our studies and understanding of the MSP emission mechanism by publishing high quality, multi-frequency polarization profiles. All the raw data and resulting averaged profiles are available for public access online.

Producing a model to describe all these observations will be extremely challenging and made more-so by the gaps in the frequency coverage that we currently have available at the Parkes telescope. In order to mitigate this problem, we are developing a new ultra-wideband receiver system that will provide simultaneous observations from ~ 700 MHz up to ~ 4 GHz. As our telescope sensitivity continues to improve, millisecond pulsar profiles seem to become more and more complicated. However, it is still likely that even more low-level components exist in these pulsars. A full understanding of the pulse profiles will only be possible with the sensitivity provided by future telescopes such as the five-hundred-metre-spherical telescope (FAST) and the Square Kilometre Array (SKA).

ACKNOWLEDGMENTS

The Parkes radio telescope is part of the Australia Telescope National Facility which is funded by the Commonwealth of Australia for operation as a National Facility managed by CSIRO. This work was supported by the Australian Research Council through grant DP140102578. GH is a recipient of a Future Fellowship from the Australian Research Council. VR is a recipient of a John Stocker postgraduate scholarship from the Science and Industry Endowment Fund of Australia. LW acknowledges support from the Australian Research Council. This work made use of NASA's ADS system.

REFERENCES

- Bhat N. D. R., Cordes J. M., Camilo F., Nice D. J., Lorimer D. R., 2004, ApJ, 605, 759
- Bhat N. D. R. et al., 2014, ApJL, 791, L32
- Burgay M. et al., 2013, MNRAS, 433, 259
- Chen J.-L., Wang H.-G., Chen W.-H., Zhang H., Liu Y., 2007, ChJAA, 7, 789
- Cordes J. M., 1978, ApJ, 222, 1006
- Cordes J. M., Shannon R. M., 2010, ArXiv e-prints
- Dyks J., Rudak B., 2003, ApJ, 598, 1201
- Dyks J., Rudak B., Demorest P., 2010, MNRAS, 401, 1781
- Everett J. E., Weisberg J. M., 2001, ApJ, 553, 341
- Foster R. S., Backer D. C., 1990, ApJ, 361, 300
- Gupta Y., Gangadhara R. T., 2003, ApJ, 584, 418
- Han J. L., Manchester R. N., 2001, MNRAS, 320, L35
- Hobbs G. et al., 2011, PASA, 28, 202
- Hobbs G. B., Edwards R. T., Manchester R. N., 2006, MNRAS, 369, 655
- Hotan A. W., van Straten W., Manchester R. N., 2004, PASA, 21, 302
- Johnston S. et al., 1993, Nature, 361, 613
- Karastergiou A., 2009, MNRAS, 392, L60
- Keith M. J. et al., 2013, MNRAS, 429, 2161
- Keith M. J. et al., 2012, MNRAS, 419, 1752
- Keith M. J. et al., 2011, MNRAS, 414, 1292
- Kennett M., Melrose D., 1998, PASA, 15, 211
- Kijak J., Lewandowski W., Maron O., Gupta Y., Jessner A., 2011, A&A, 531, A16
- Kramer M., 1994, A&AS, 107, 527
- Kramer M., Lange C., Lorimer D. R., Backer D. C., Xilouris K. M., Jessner A., Wielebinski R., 1999a, ApJ, 526, 957
- Kramer M., Wielebinski R., Jessner A., Gil J. A., Seiradakis J. H., 1994, A&AS, 107, 515
- Kramer M. et al., 1999b, ApJ, 520, 324
- Kramer M., Xilouris K. M., Jessner A., Wielebinski R., Timofeev M., 1996, A&A, 306, 867
- Kramer M., Xilouris K. M., Lorimer D. R., Doroshenko O., Jessner A., Wielebinski R., Wolszczan A., Camilo F., 1998, ApJ, 501, 270
- Kuzmin A. D., Losovsky B. Y., 2001, A&A, 368, 230
- Liu K. et al., 2014, MNRAS, 443, 3752
- Lorimer D. R., Kramer M., 2005, Handbook of Pulsar Astronomy. Cambridge University Press
- Lorimer D. R., Yates J. A., Lyne A. G., Gould D. M., 1995, MNRAS, 273, 411
- Lyne A. G., Brinklow A., Middleditch J., Kulkarni S. R., Backer D. C., 1987, Nature, 328, 399
- Lyne A. G., Manchester R. N., 1988, MNRAS, 234, 477
- Manchester R. N., 1995, Journal of Astrophysics and Astronomy, 16, 107
- Manchester R. N., 2005, ApSS, 297, 101
- Manchester R. N., Han J. L., 2004, ApJ, 609, 354
- Manchester R. N. et al., 2013, PASA, 30, 17
- Manchester R. N., Hobbs G. B., Teoh A., Hobbs M., 2005, Astron. J., 129, 1993
- Manchester R. N., Johnston S., 1995, ApJL, 441, L65
- Maron O., Kijak J., Kramer M., Wielebinski R., 2000, A&AS, 147, 195
- Navarro J., Manchester R. N., Sandhu J. S., Kulkarni S. R., Bailes M., 1997, ApJ, 486, 1019
- Noutsos A., Karastergiou A., Kramer M., Johnston S., Stappers B. W., 2009, MNRAS, 396, 1559
- Ord S. M., van Straten W., Hotan A. W., Bailes M., 2004, MNRAS, 352, 804
- Olsowski S., van Straten W., Bailes M., Jameson A., Hobbs G., 2014, MNRAS, 441, 3148
- Pennucci T. T., Demorest P. B., Ransom S. M., 2014, ApJ, 790, 93
- Petrova S. A., 2002, A&A, 383, 1067
- Radhakrishnan V., Cooke D. J., 1969, Astrophys. Lett., 3, 225
- Ramachandran R., Backer D. C., Rankin J. M., Weisberg J. M., Devine K. E., 2004, ApJ, 606, 1167
- Rankin J. M., 1993, ApJ, 405, 285
- Ravi V., Manchester R. N., Hobbs G., 2010, ApJL, 716, L85
- Shannon R. M. et al., 2014, ArXiv e-prints
- Shannon R. M. et al., 2013, Science, 342, 334
- Stairs I. H., Thorsett S. E., Camilo F., 1999, ApJS, 123, 627
- Taylor J. H., 1992, Royal Society of London Philosophical Transactions Series A, 341, 117
- Thorsett S. E., 1991, ApJ, 377, 263
- Thorsett S. E., Stinebring D. R., 1990, ApJ, 361, 644
- Toscano M., Bailes M., Manchester R. N., Sandhu J. S., 1998, ApJ, 506, 863
- van Straten W., 2004, ApJS, 152, 129
- van Straten W., Manchester R. N., Johnston S., Reynolds J. E., 2010, PASA, 27, 104
- Wang C., Han J. L., Lai D., 2011, MNRAS, 417, 1183
- Wang J. B. et al., 2014, ArXiv e-prints

- Watters K. P., Romani R. W., Weltevrede P., Johnston S., 2009, ApJ, 695, 1289
- Xilouris K. M., Kramer M., Jessner A., von Hoensbroech A., Lorimer D., Wielebinski R., Wolszczan A., Camilo F., 1998, ApJ, 501, 286
- Yan W. M. et al., 2011a, ApSS, 335, 485
- Yan W. M. et al., 2011b, MNRAS, 414, 2087
- Zhu X.-J. et al., 2014, MNRAS, 444, 3709

APPENDIX A: MULTI-FREQUENCY POLARIZATION PROFILES

In this section, we present the multi-frequency polarization profiles and phase-resolved studies for each MSPs. Detailed descriptions of the figures and specific comments on the processing for each individual pulsar have been presented in Section 3.

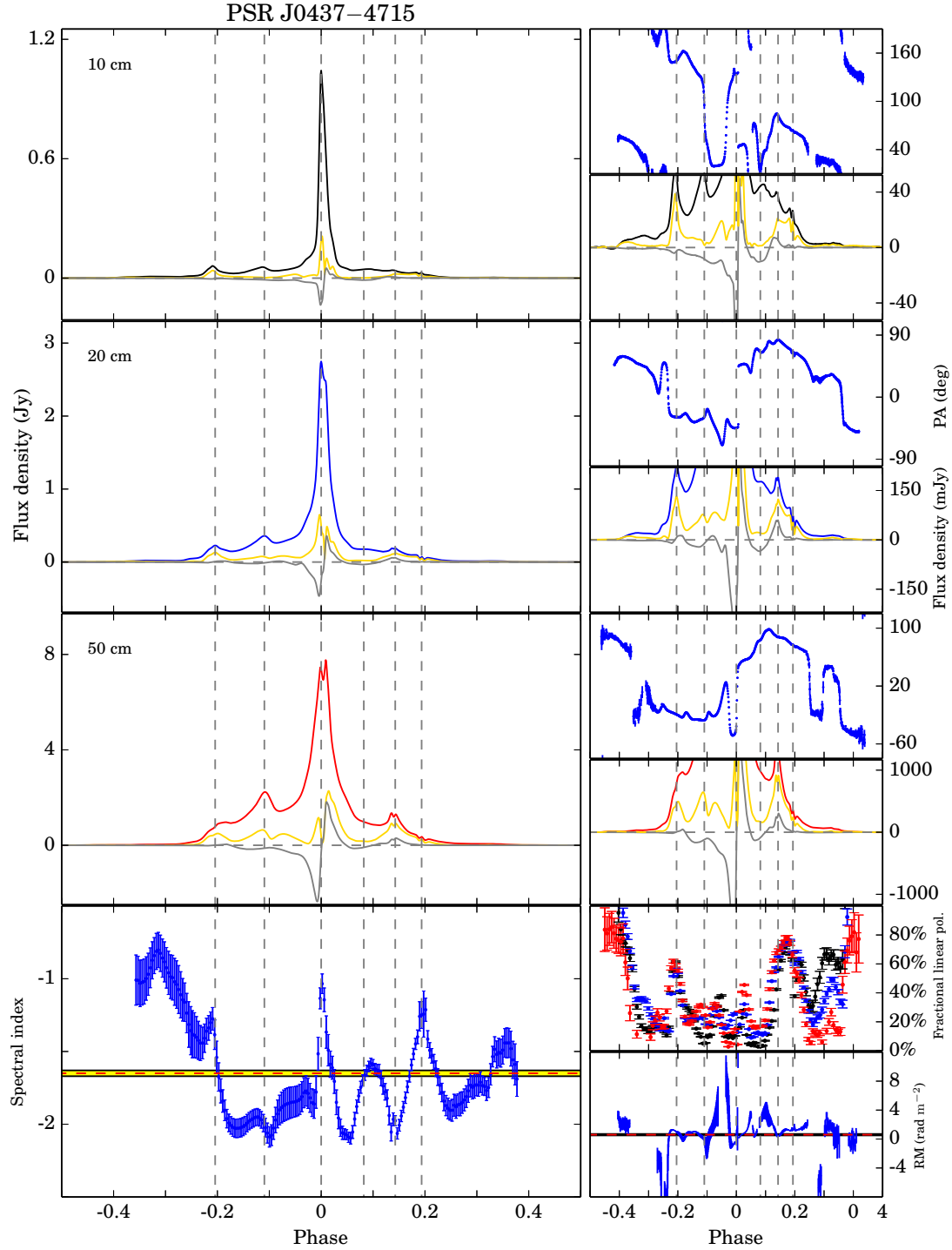


Figure A1. Multi-frequency polarization profiles and phase-resolved results for PSR J0437–4715. The left-hand panels show the pulse profile in the 10 cm (top), 20 cm (second panel) and 50 cm (third panel) observing bands. The black, blue and red lines in these panels respectively indicate the total intensity, Stokes I, profile in the three bands. The brown line indicates linear polarisation and the grey line shows circular polarisation. The bottom panel on the left-hand side presents the phase-resolved spectral index. The red dashed line and yellow highlighted region represent the measured spectral index and its uncertainty as presented in Table `reftableFlux`. In the right-hand panels we have two panels for each of the 10 cm, 20 cm and 50 cm bands. The upper panel shows the position angle of the linear polarisation (in degrees). The lower panels shows a zoom-in around the profile baseline to show weak profile features. The colour scheme is the same as in the left-hand panels. The bottom two panels on the right-hand side show the phase-resolved fractional linear polarisation for the three observing bands using the same colour scheme as above, and the phase-resolved RM. The red dashed line and yellow highlighted region represent the measured RM value and its uncertainty. In all panels, vertical dashed lines show the positions of peaks in the 20 cm total intensity profile.

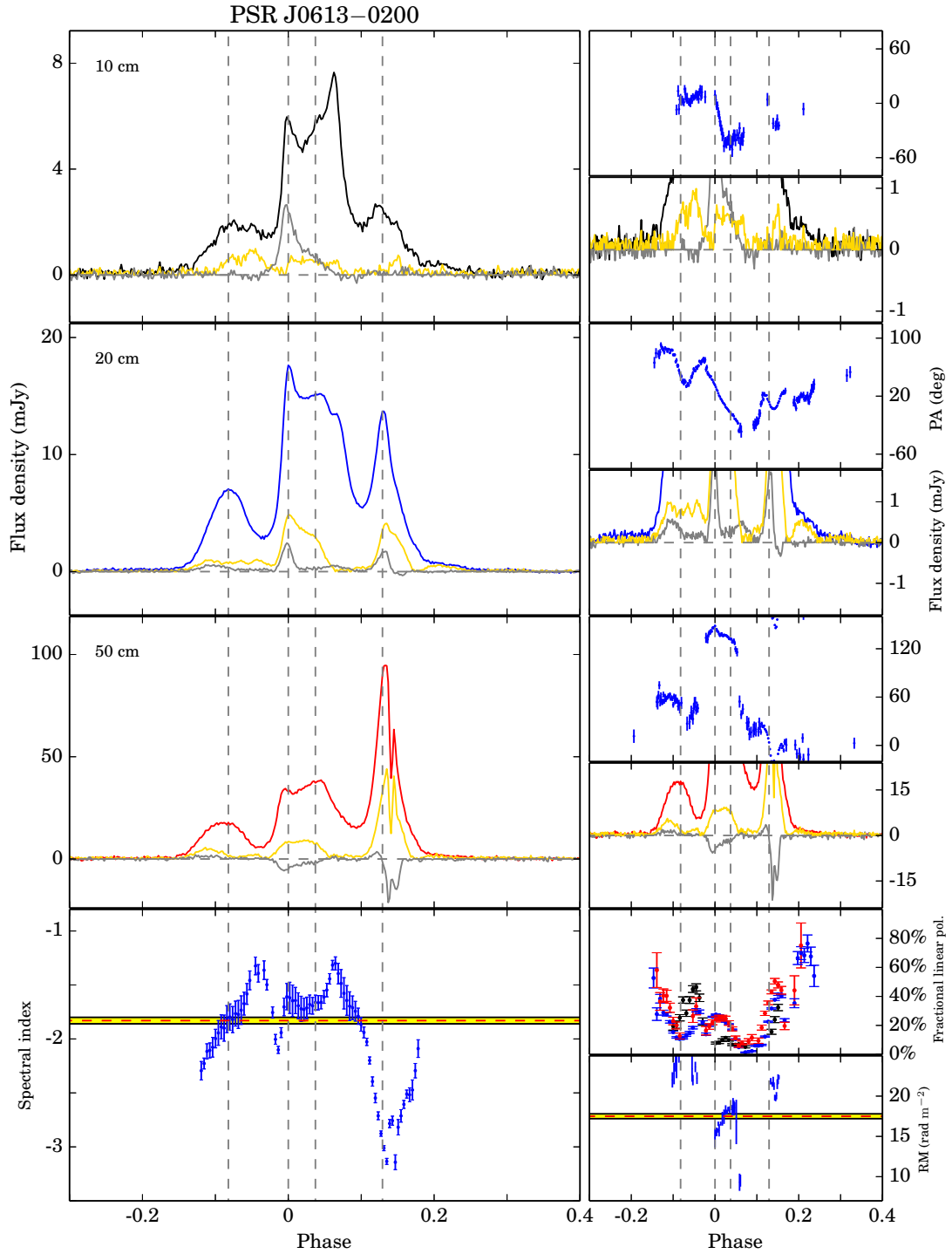


Figure A2. Multi-frequency polarization profiles for PSR J0613–0200. See Fig. A1 for further details.

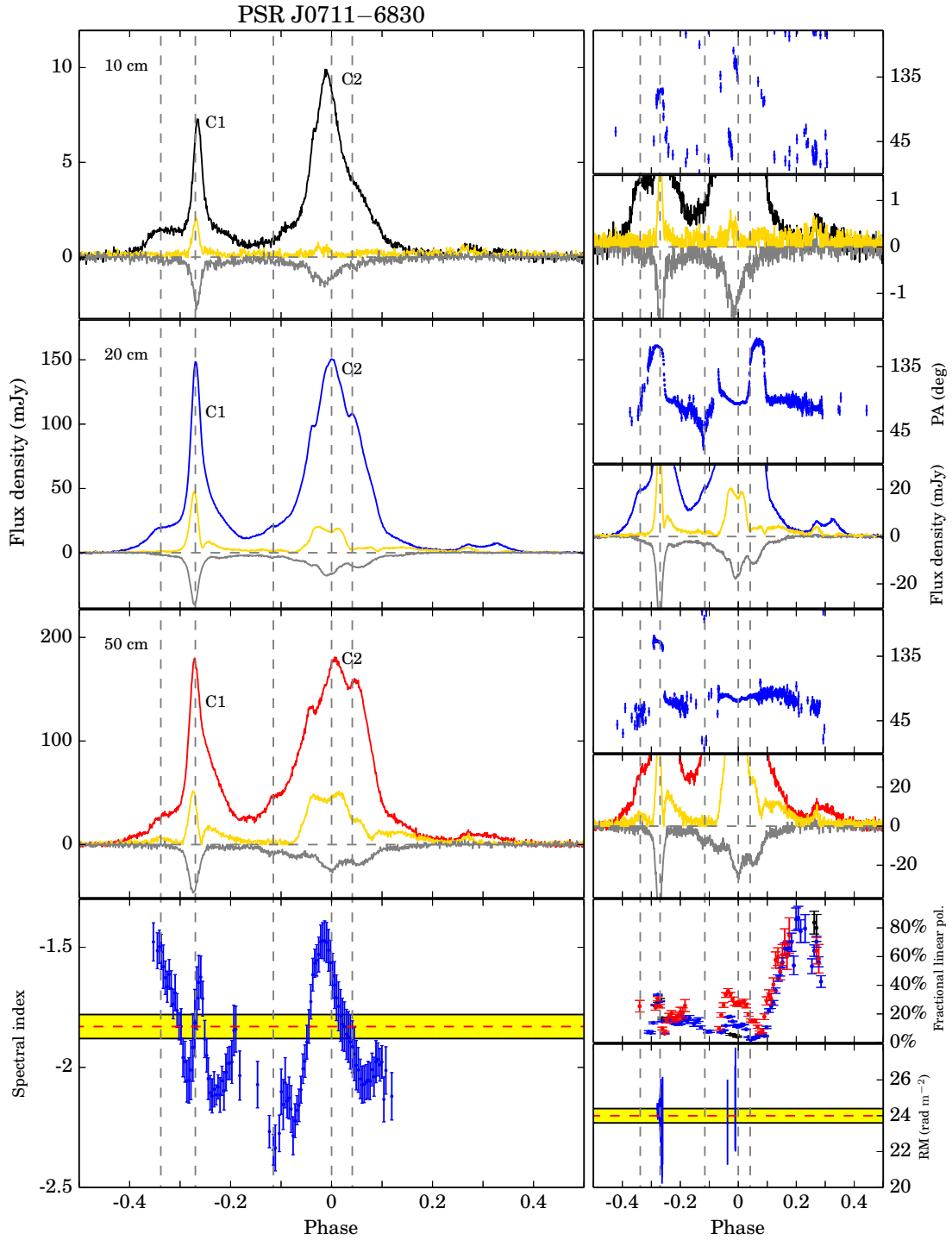


Figure A3. Multi-frequency polarization profiles for PSR J0711–6830. See Fig. A1 for further details.

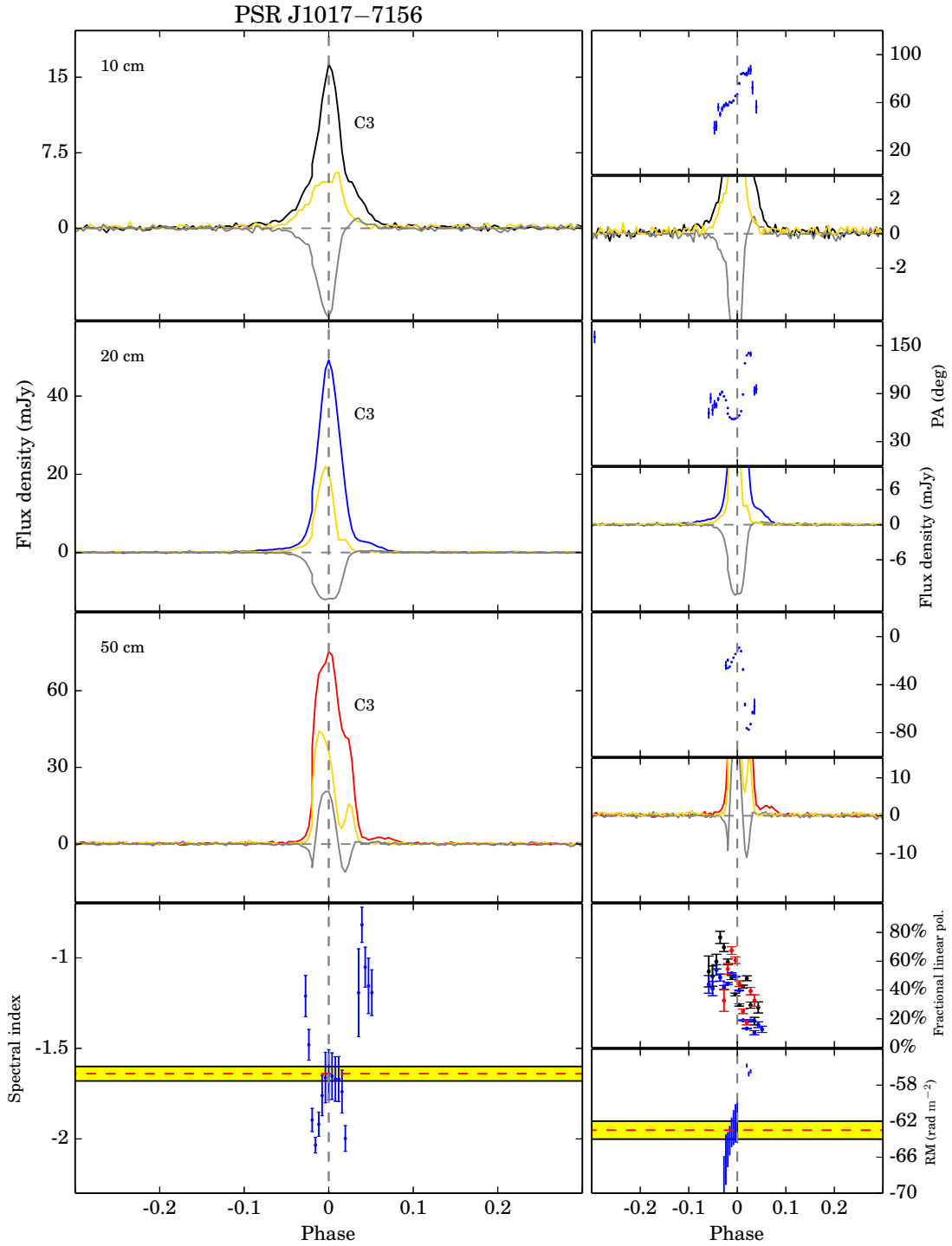


Figure A4. Multi-frequency polarization profiles for PSR J1017–7156. See Fig. A1 for further details.

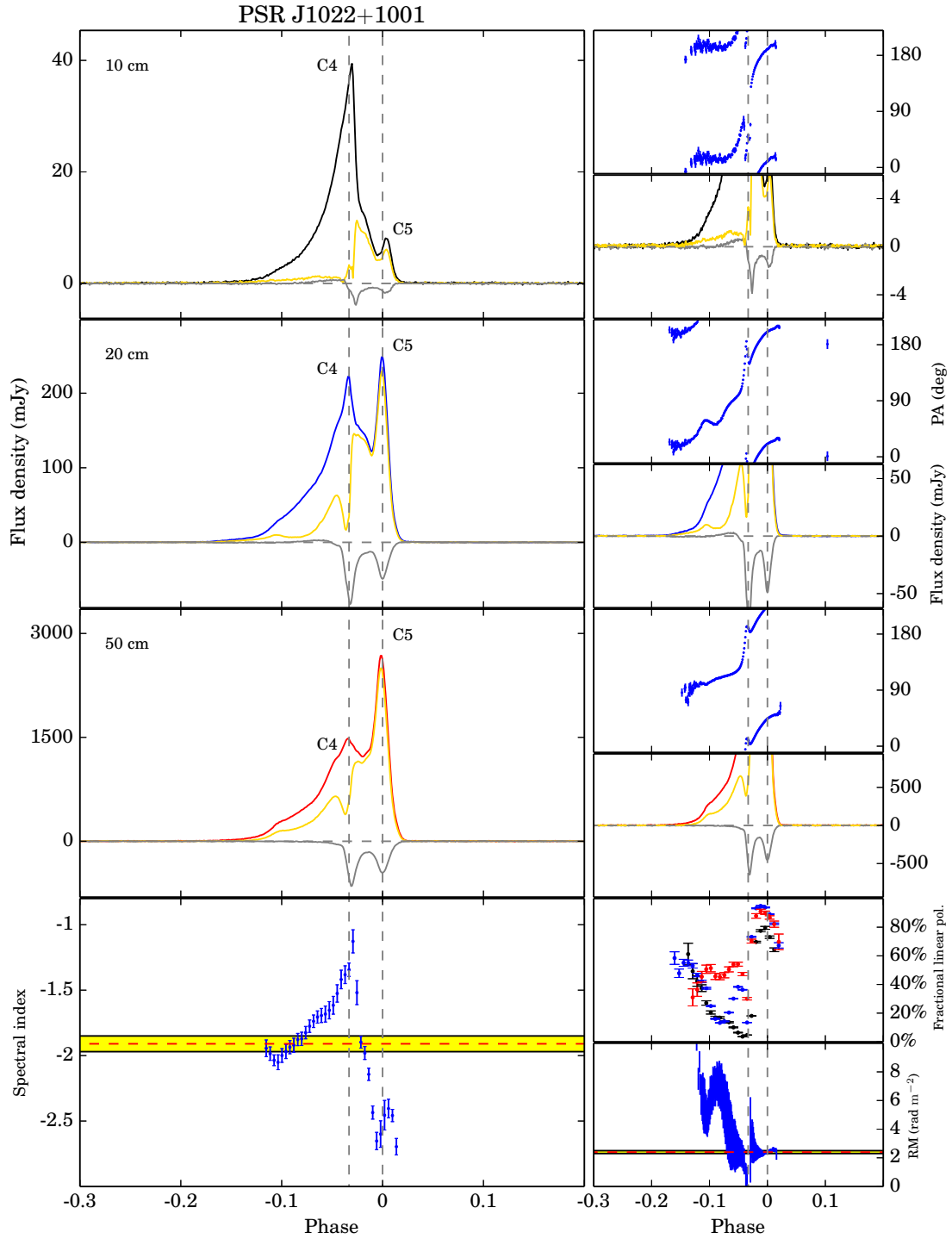


Figure A5. Multi-frequency polarization profiles for PSR J1022+1001. See Fig. A1 for further details.

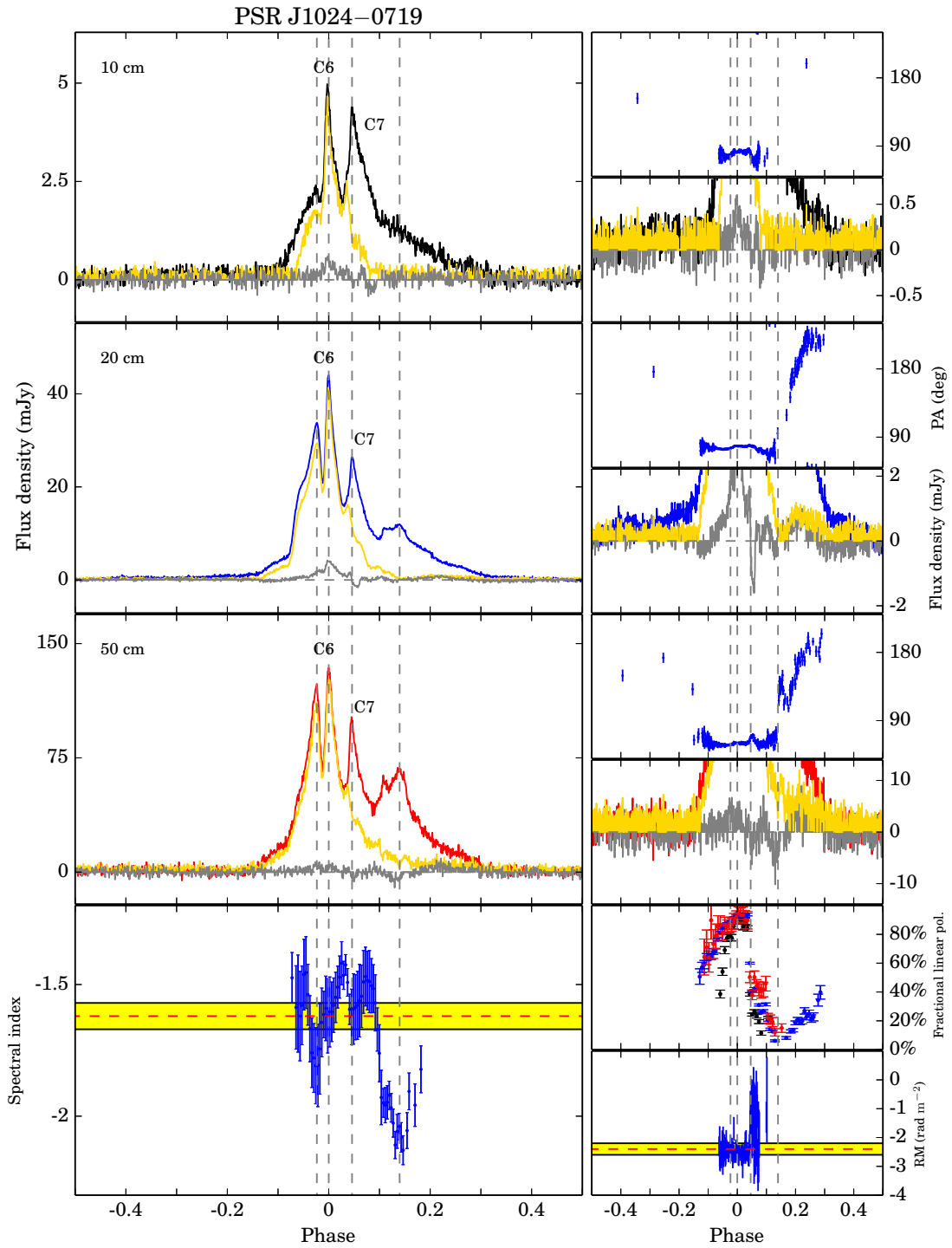


Figure A6. Multi-frequency polarization profiles for PSR J1024–0719. See Fig. A1 for further details.

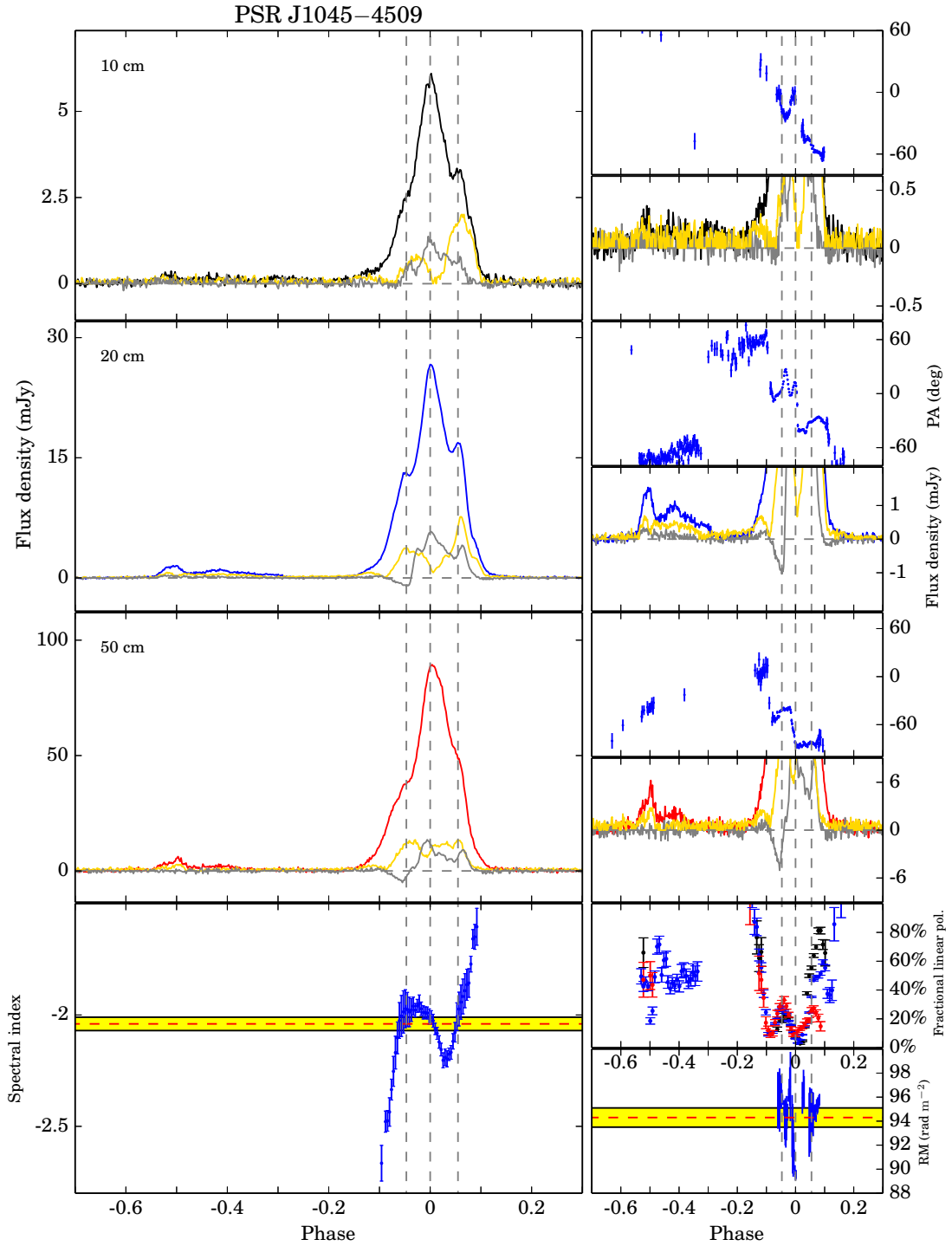


Figure A7. Multi-frequency polarization profiles for PSR J1045–4509. See Fig. A1 for further details.

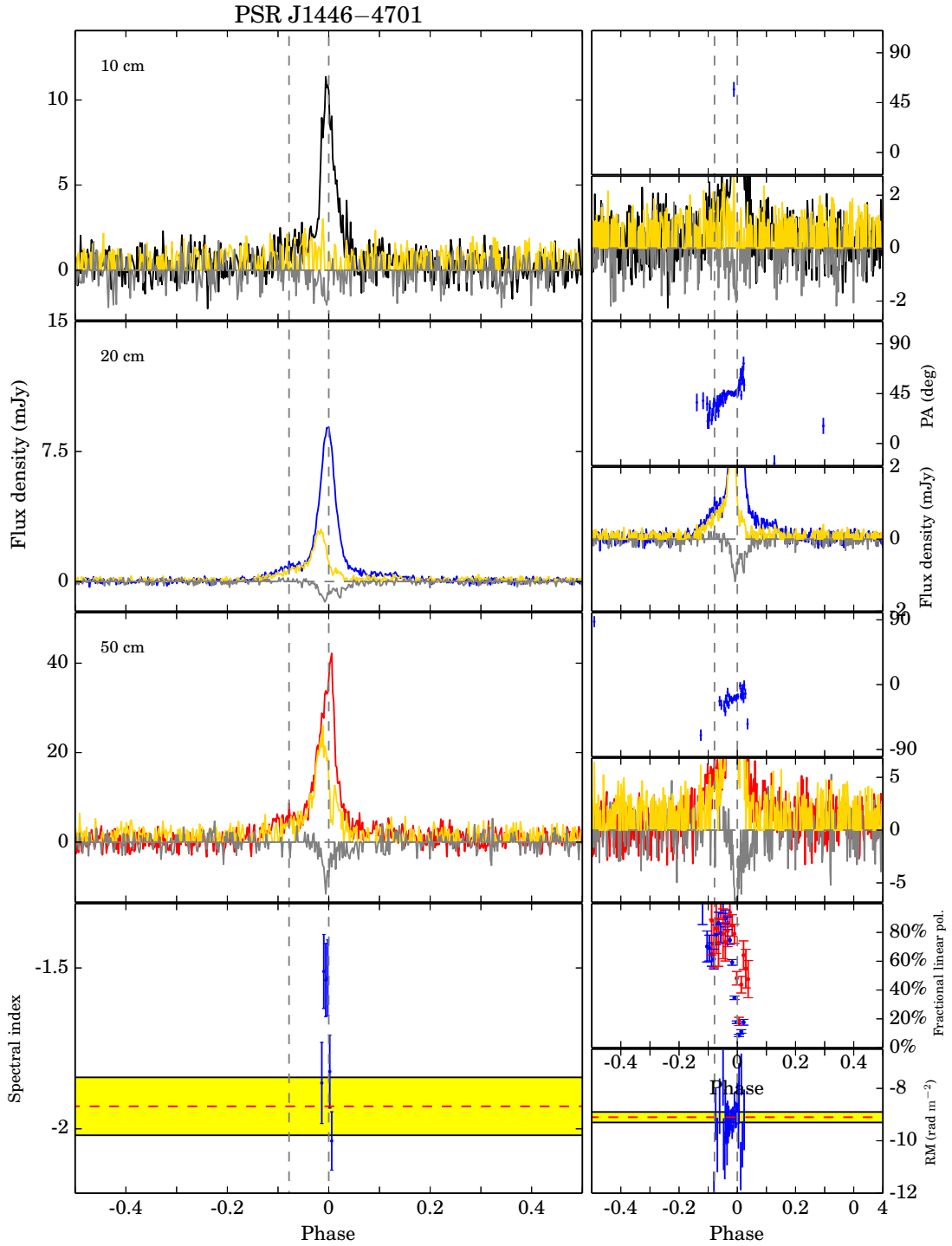


Figure A8. Multi-frequency polarization profiles for PSR J1446–4701. See Fig. A1 for further details.

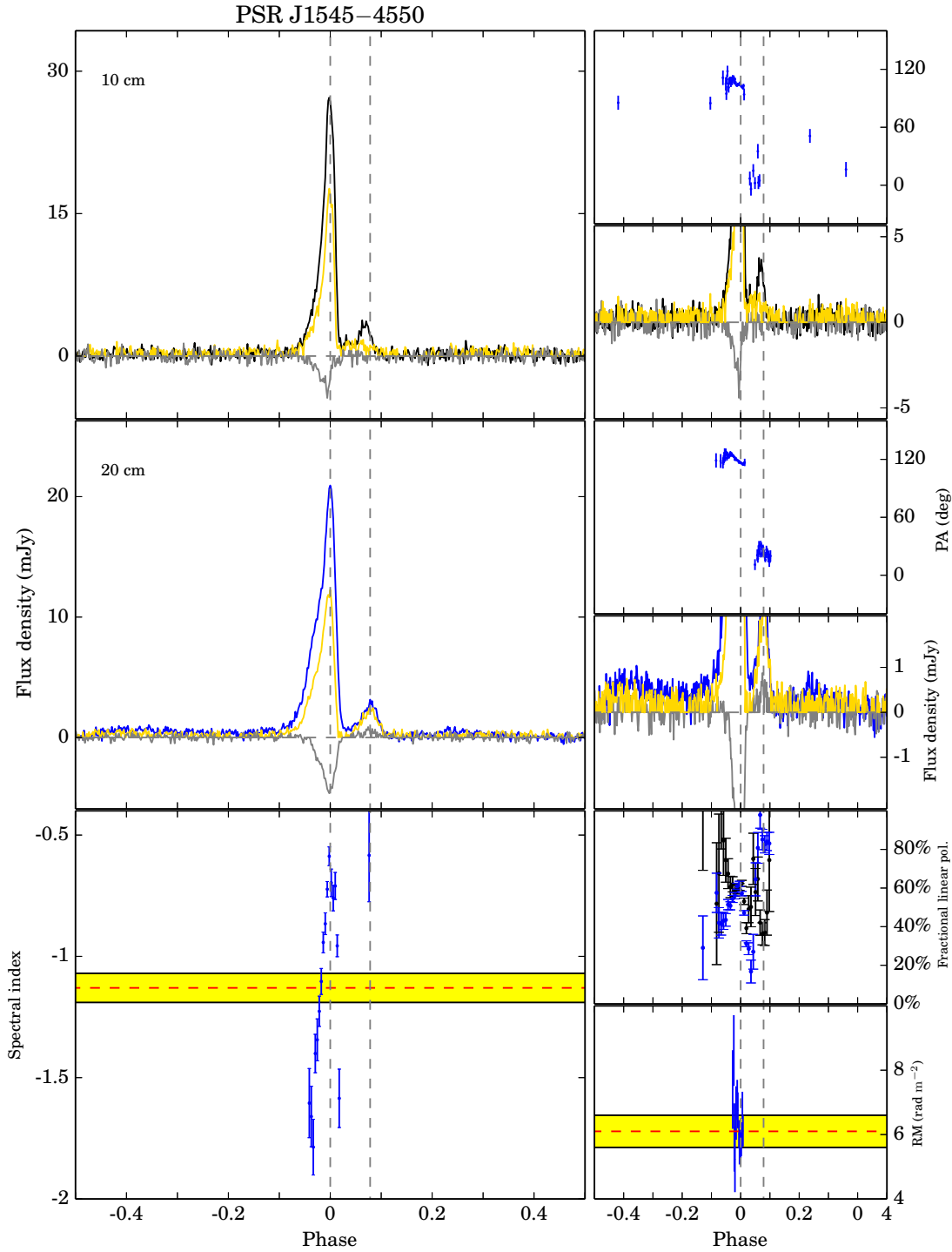


Figure A9. Multi-frequency polarization profiles for PSR J1545–4550. See Fig. A1 for further details.

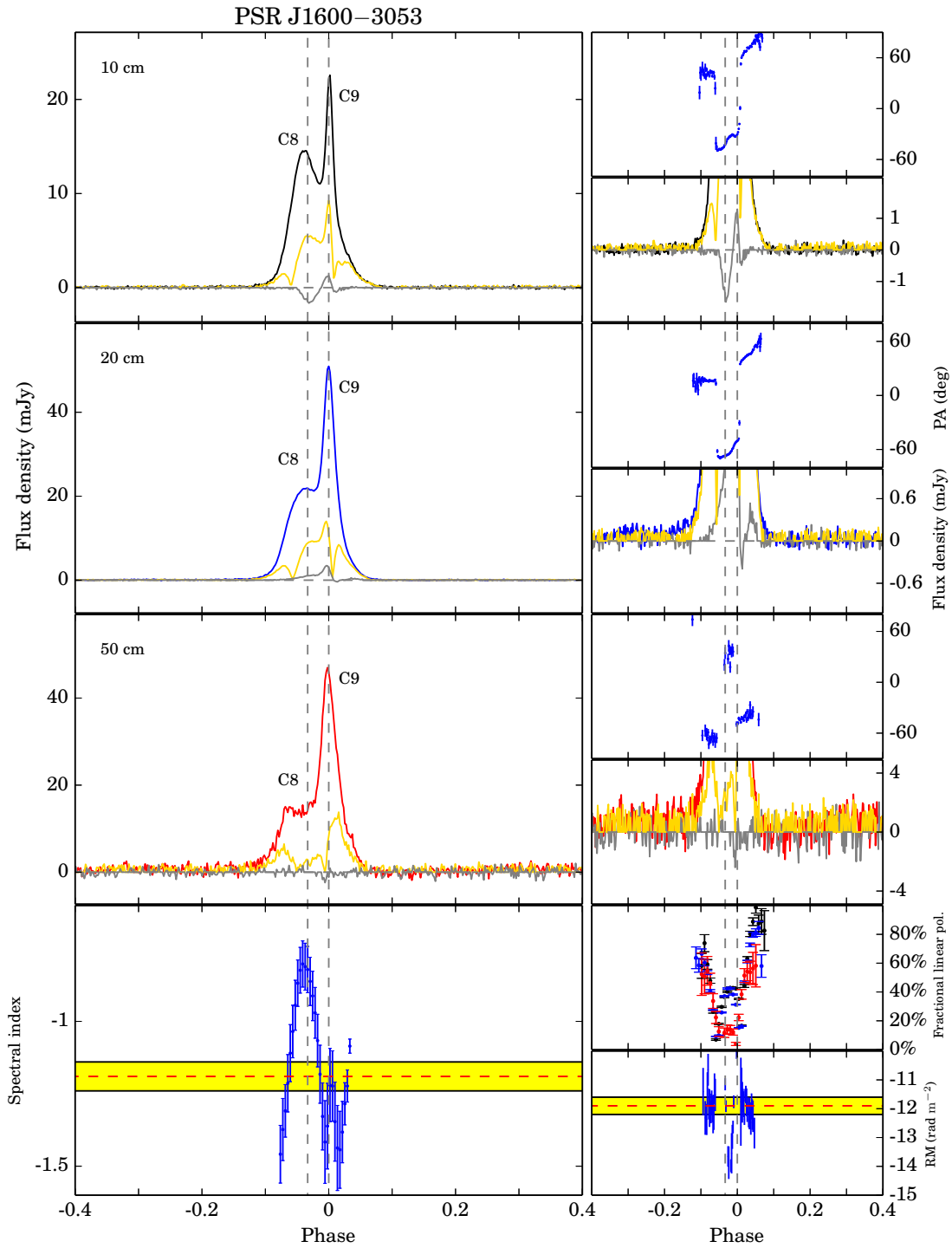


Figure A10. Multi-frequency polarization profiles for PSR J1600–3053. See Fig. A1 for further details.

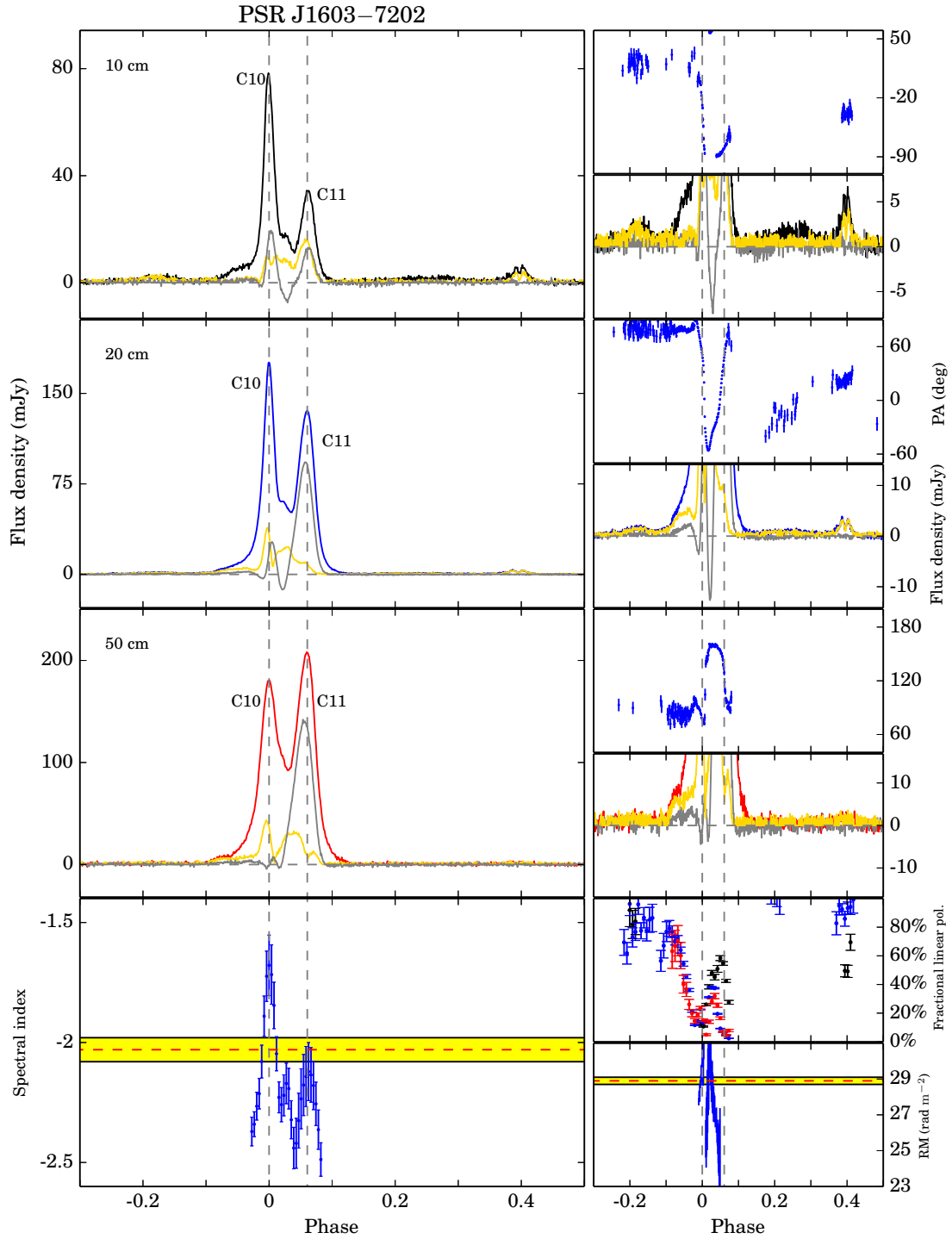


Figure A11. Multi-frequency polarization profiles for PSR J1603–7202. See Fig. A1 for further details.

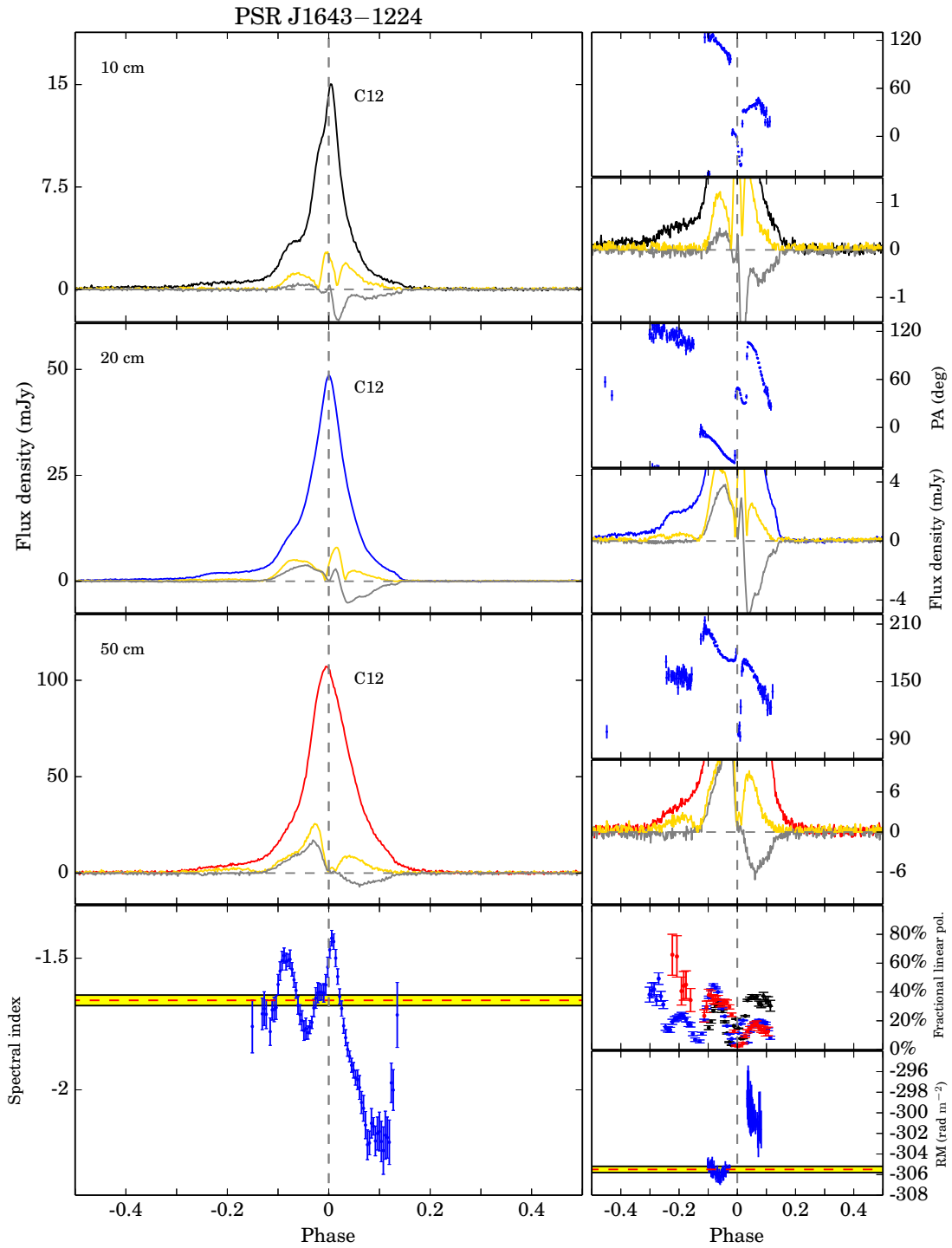


Figure A12. Multi-frequency polarization profiles for PSR J1643–1224. See Fig. A1 for further details.

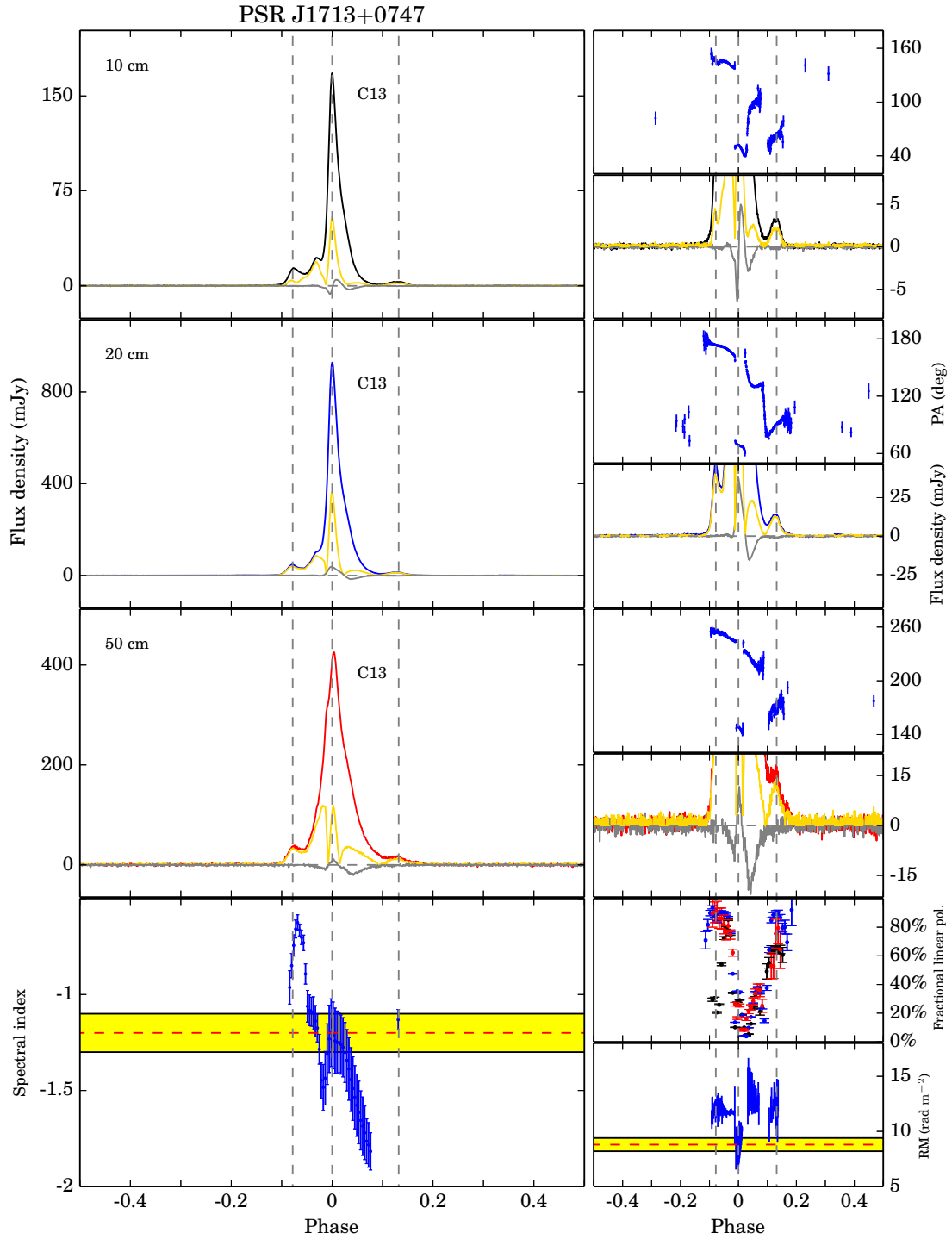


Figure A13. Multi-frequency polarization profiles for PSR J1713+0747. See Fig. A1 for further details.

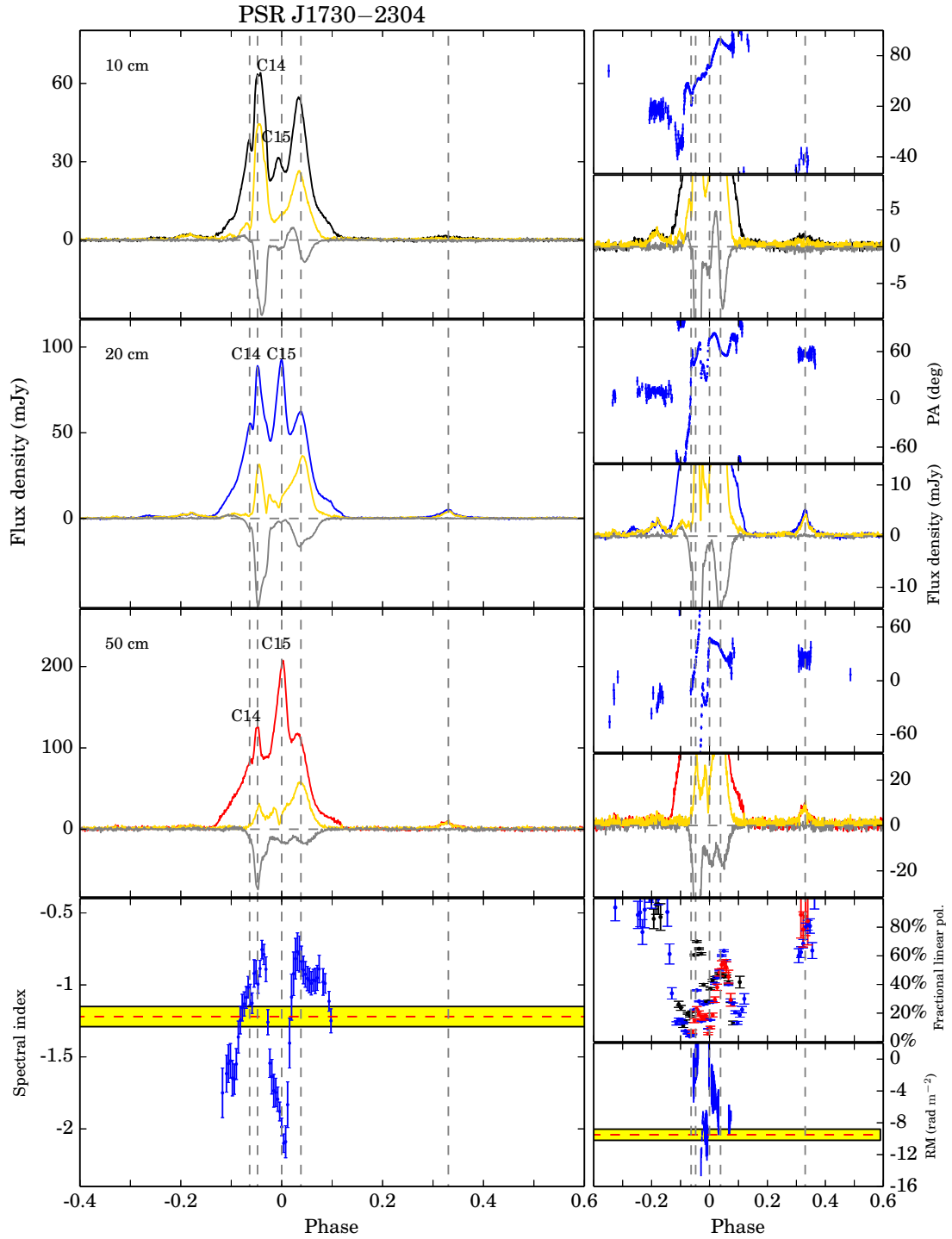


Figure A14. Multi-frequency polarization profiles for PSR J1730–2304. See Fig. A1 for further details.

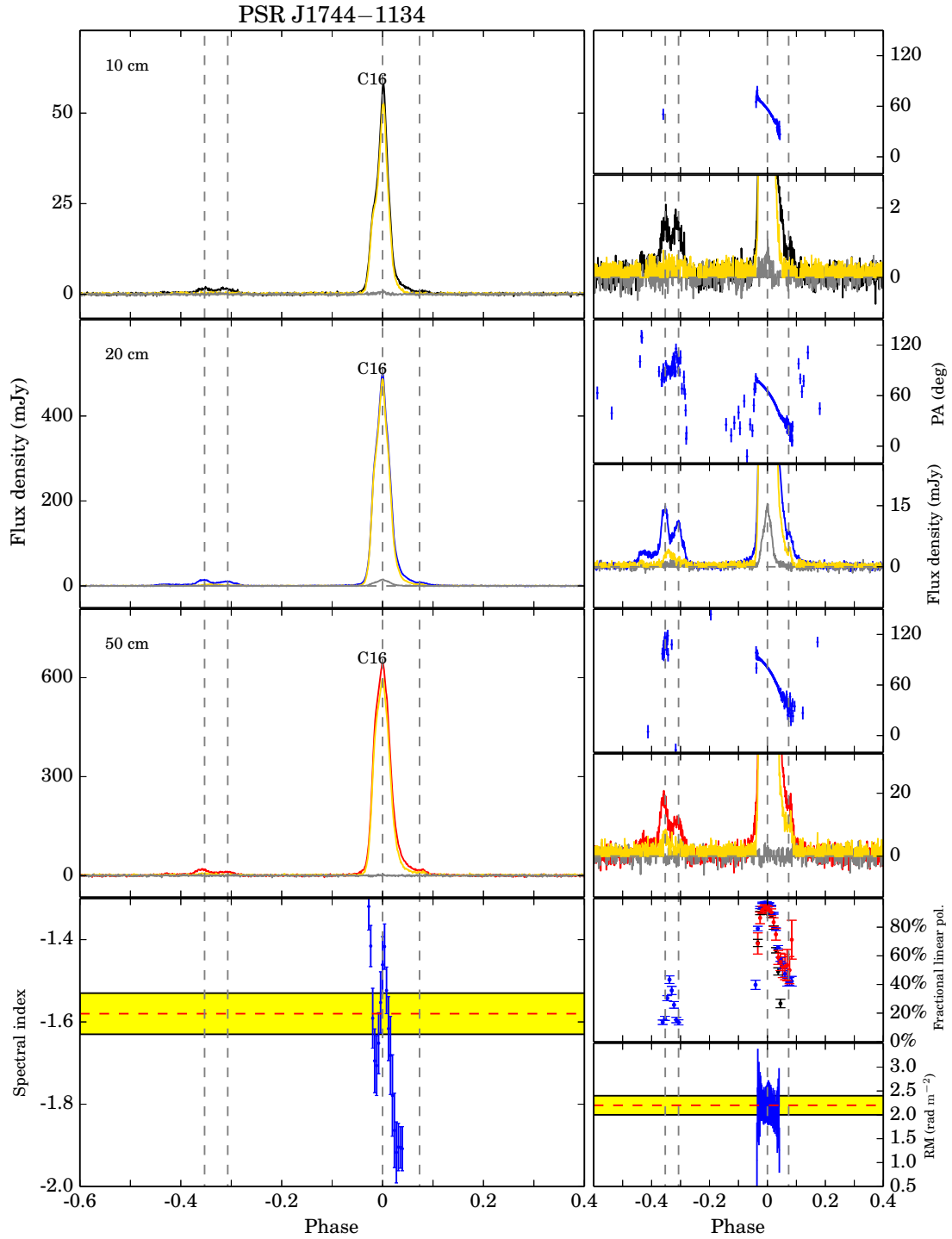


Figure A15. Multi-frequency polarization profiles for PSR J1744–1134. See Fig. A1 for further details.

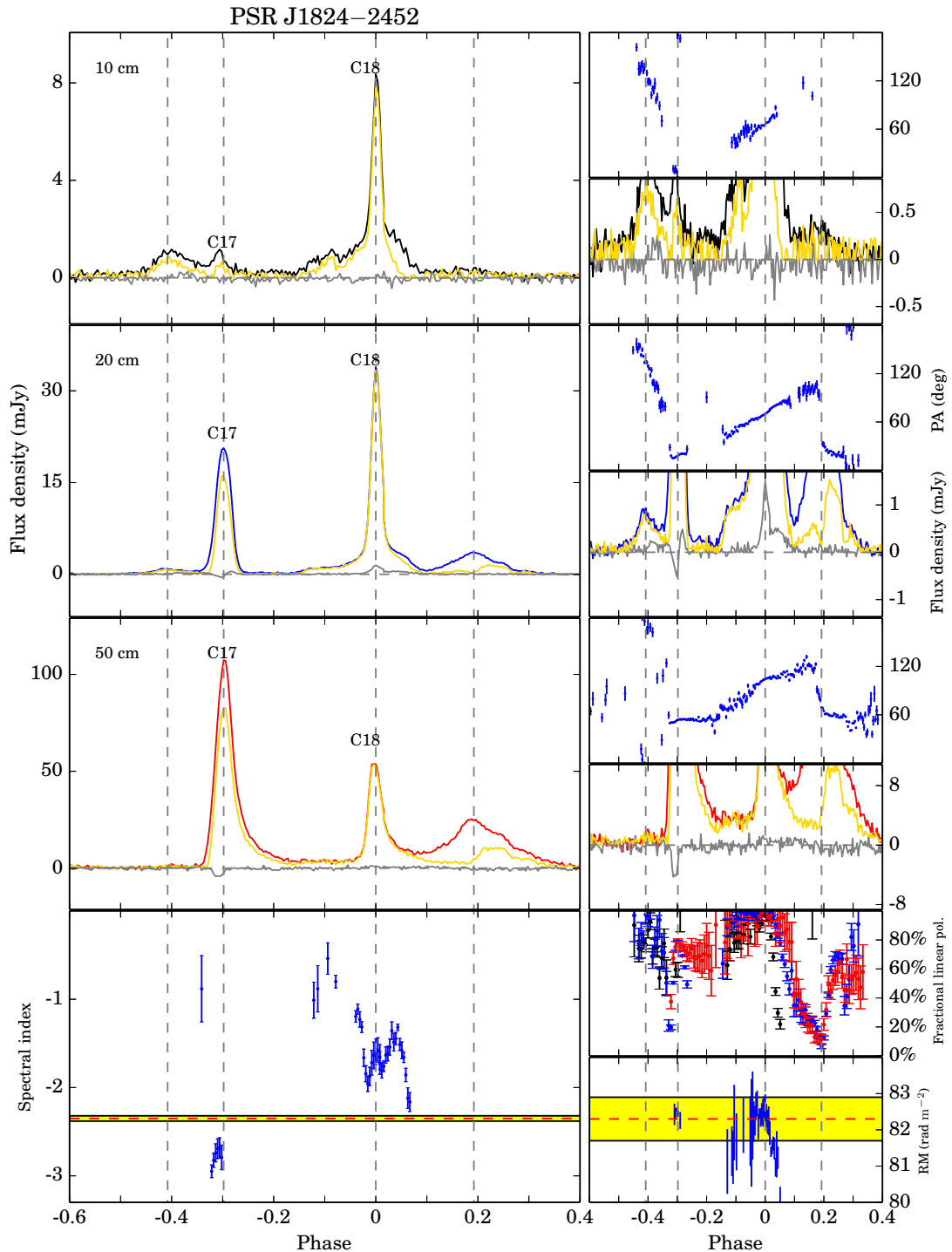


Figure A16. Multi-frequency polarization profiles for PSR J1824–2452A. See Fig. A1 for further details.

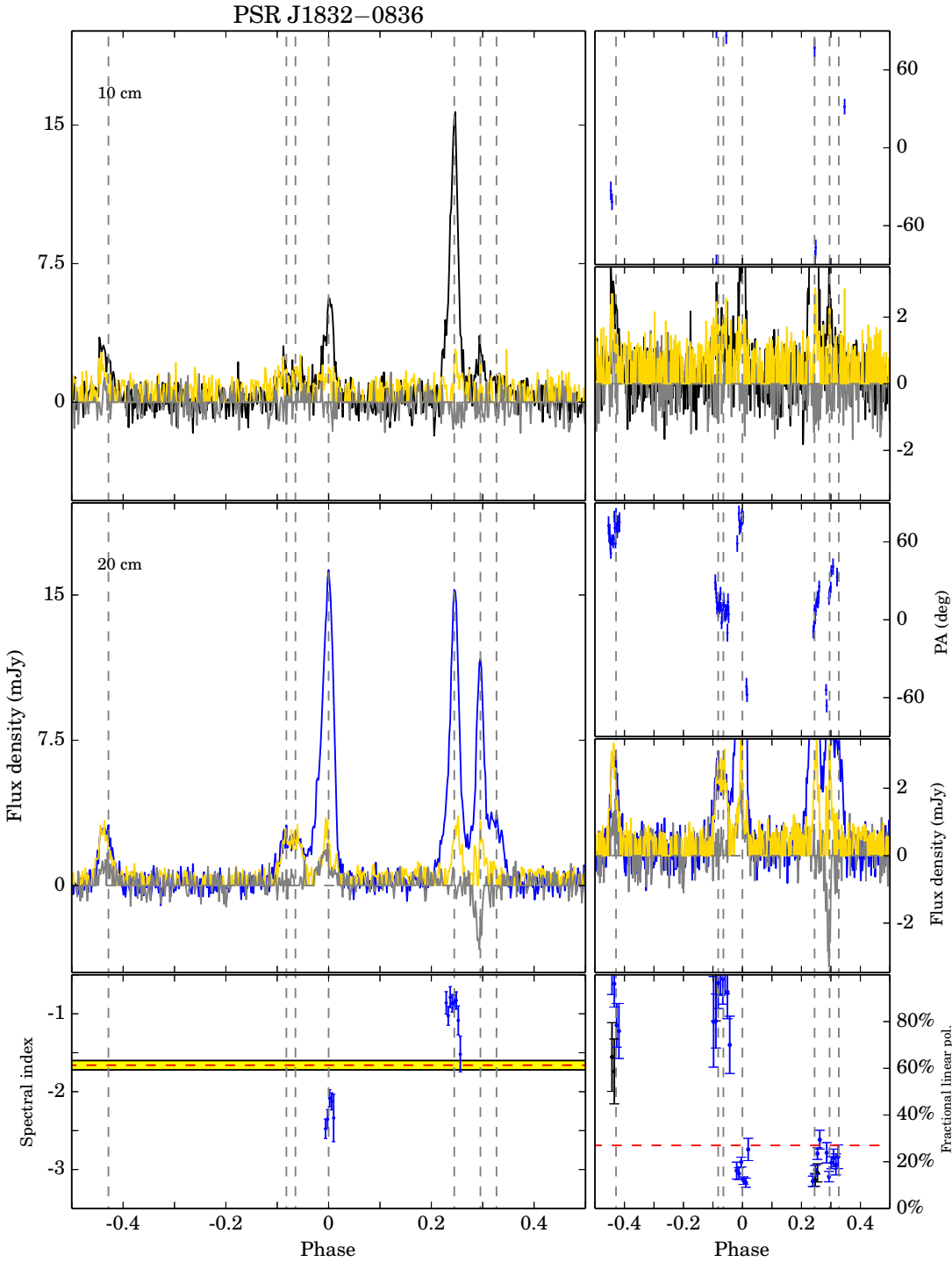


Figure A17. Multi-frequency polarization profiles for PSR J1832–0836. See Fig. A1 for further details.

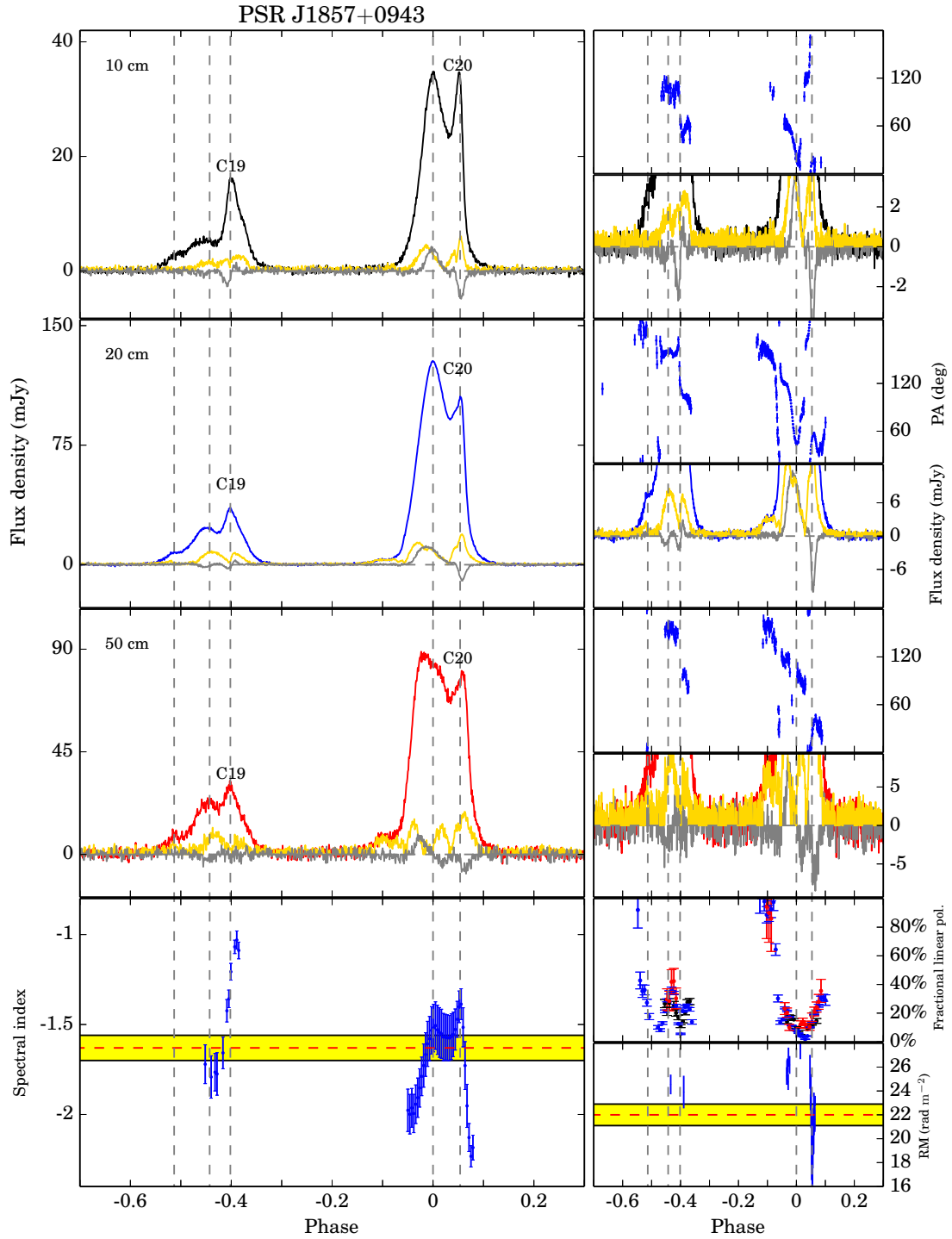


Figure A18. Multi-frequency polarization profiles for PSR J1857+0943. See Fig. A1 for further details.

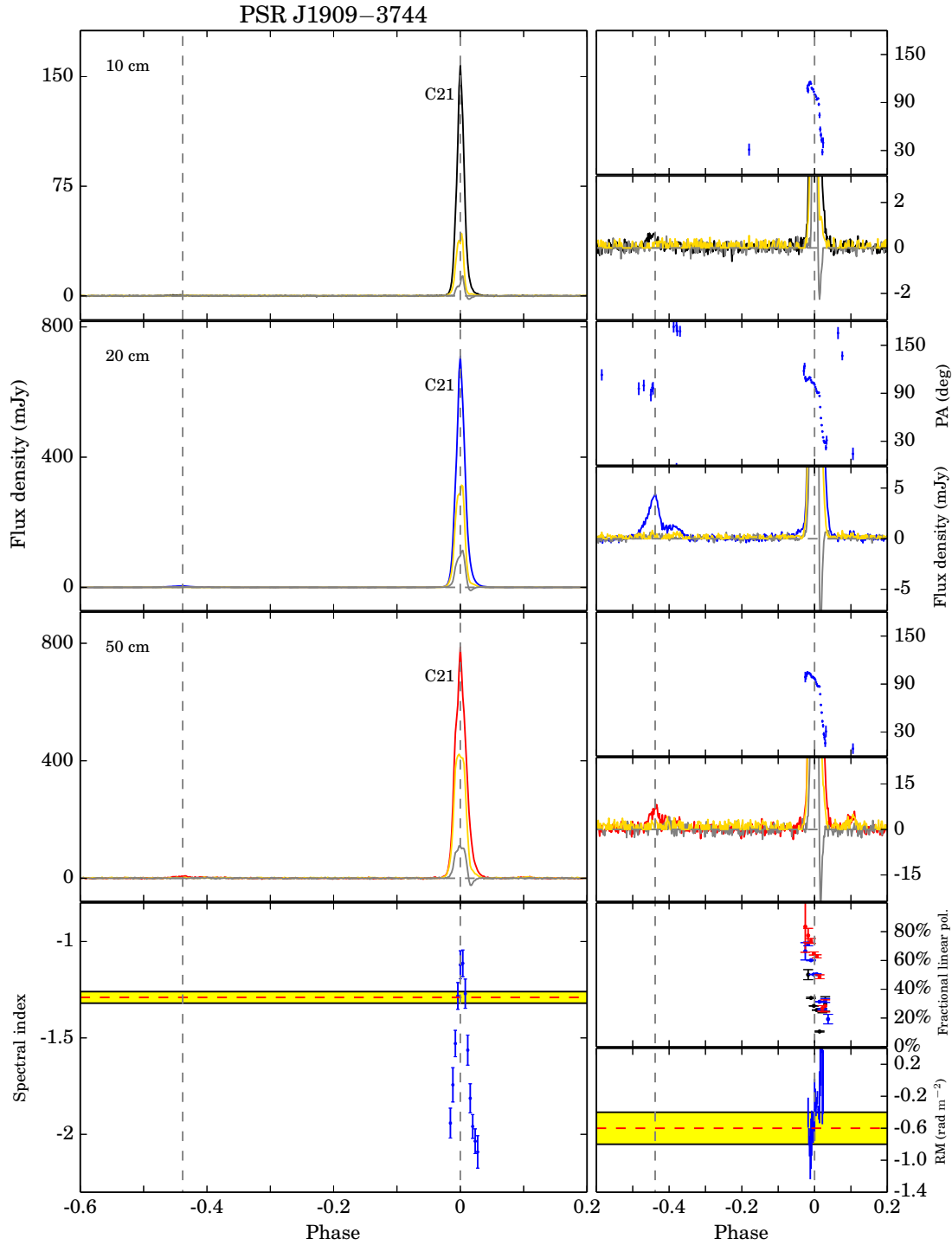


Figure A19. Multi-frequency polarization profiles for PSR J1909–3744. See Fig. A1 for further details.

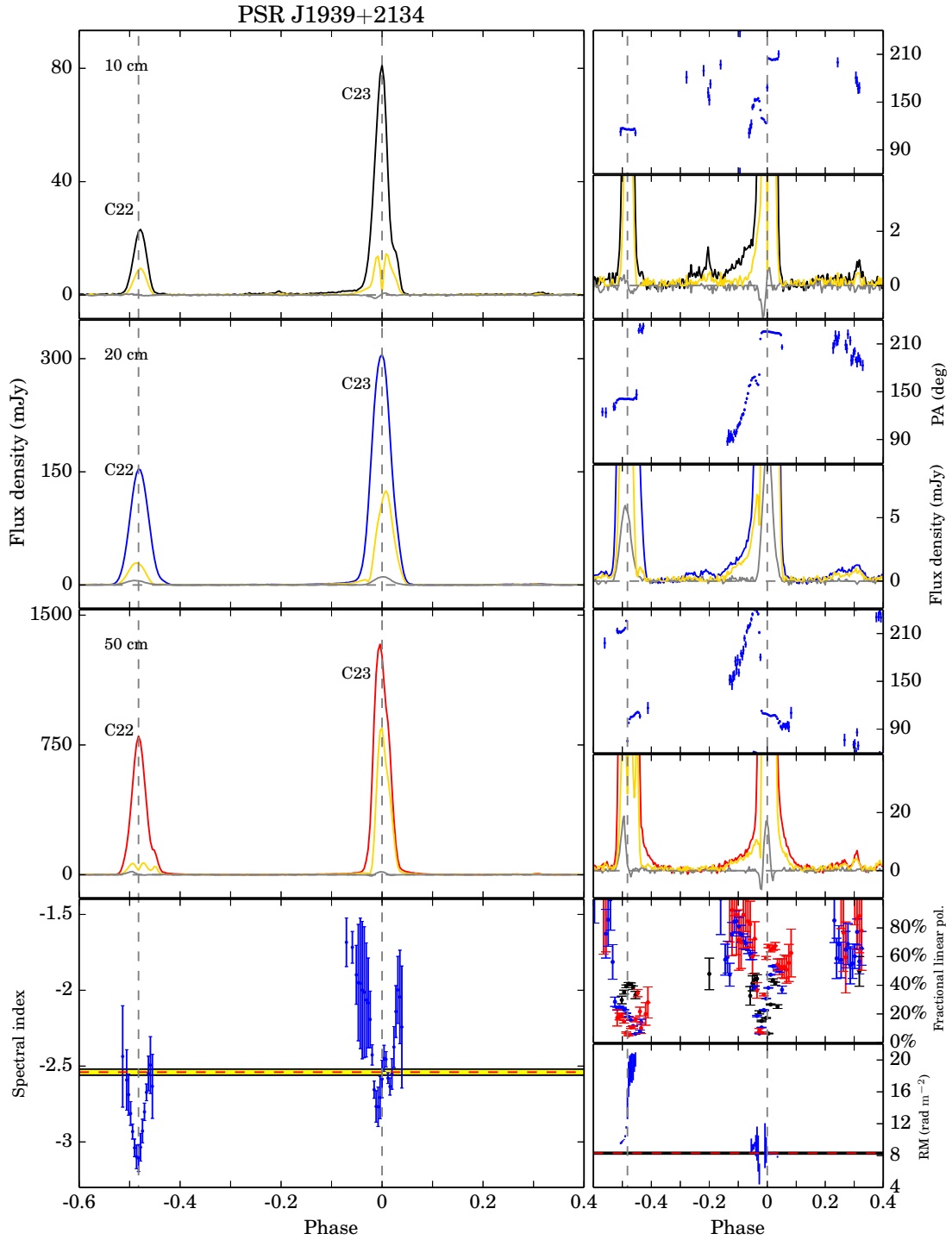


Figure A20. Multi-frequency polarization profiles for PSR J1939+2134. See Fig. A1 for further details.

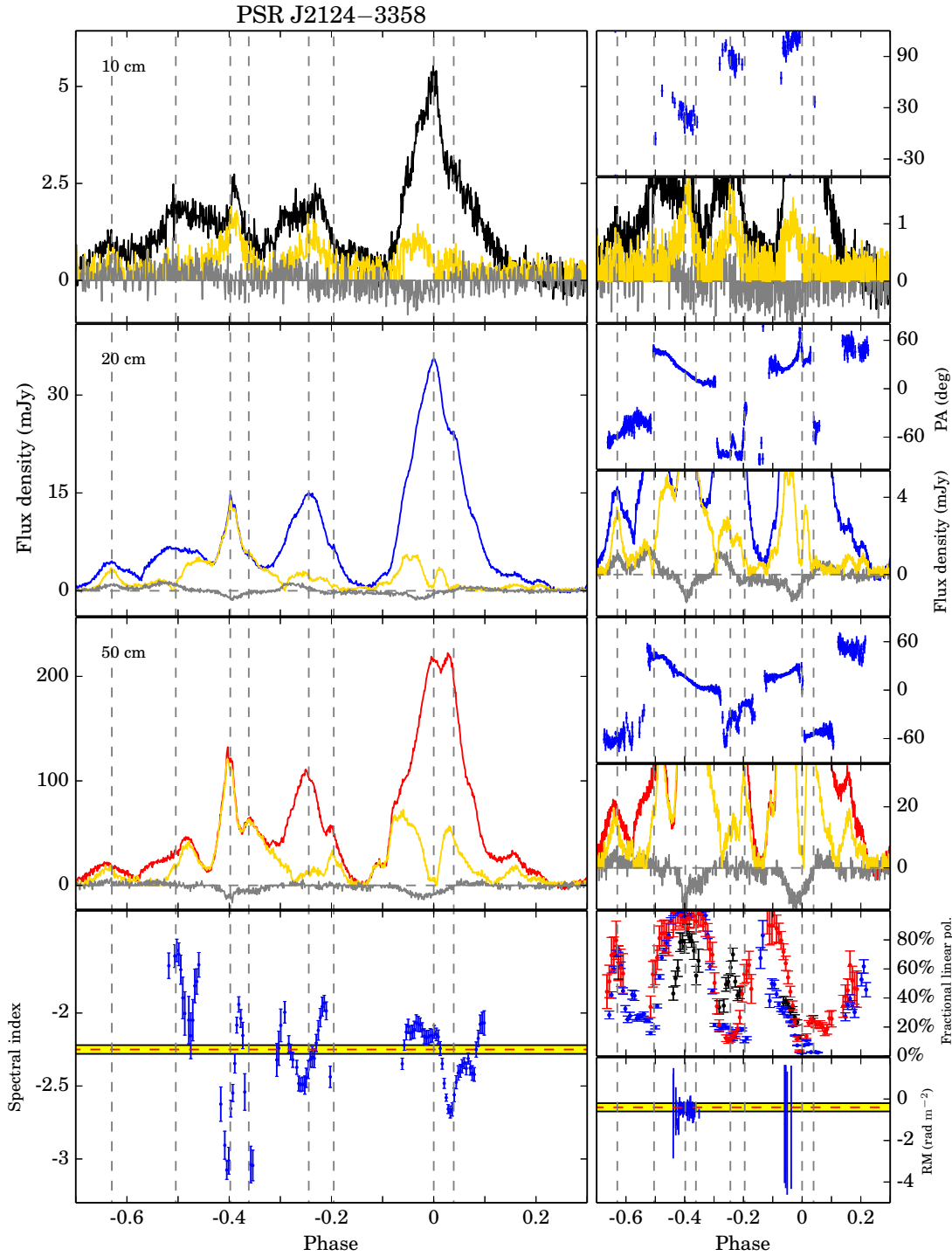


Figure A21. Multi-frequency polarization profiles for PSR J2124–3358. See Fig. A1 for further details.

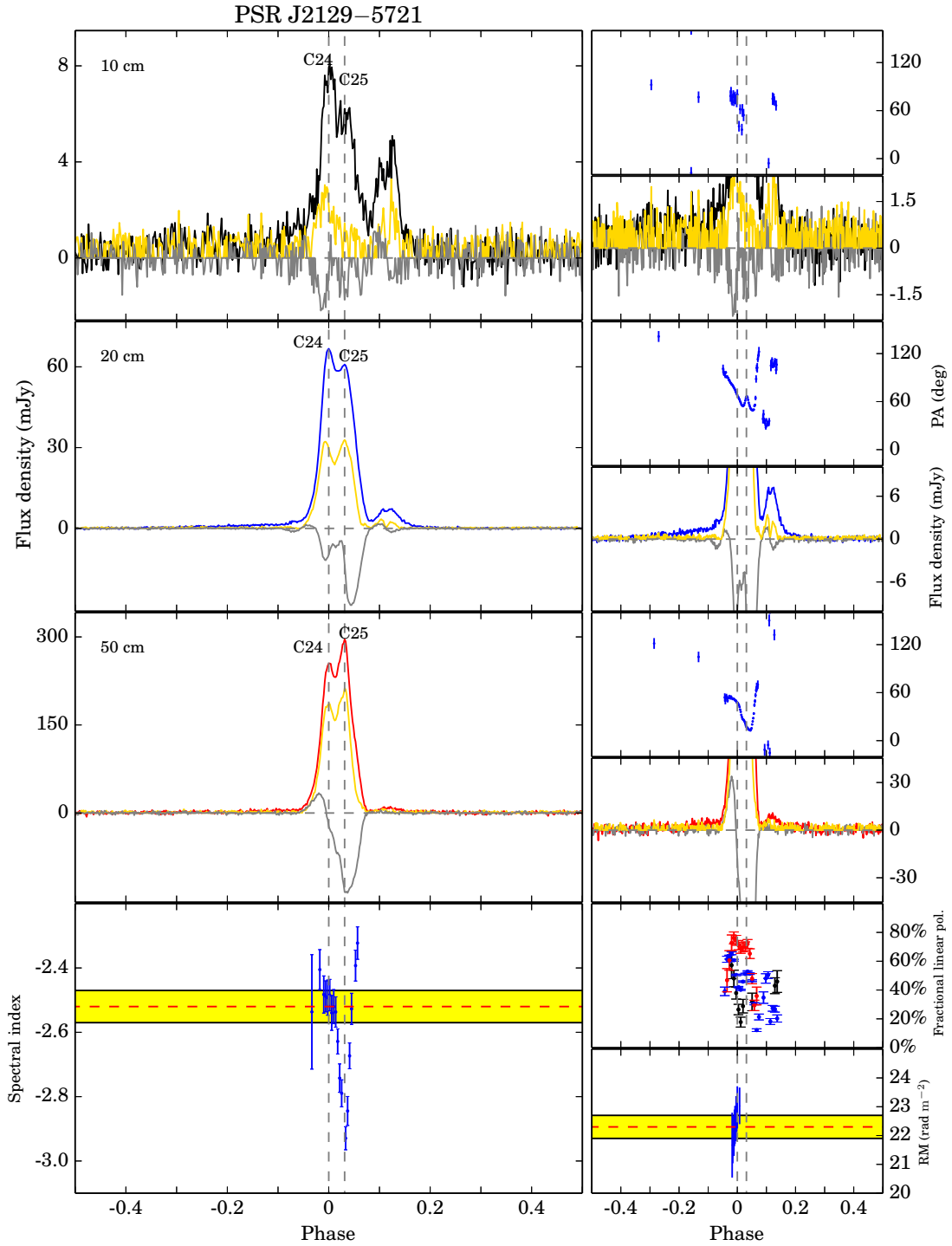


Figure A22. Multi-frequency polarization profiles for PSR J2129–5721. See Fig. A1 for further details.

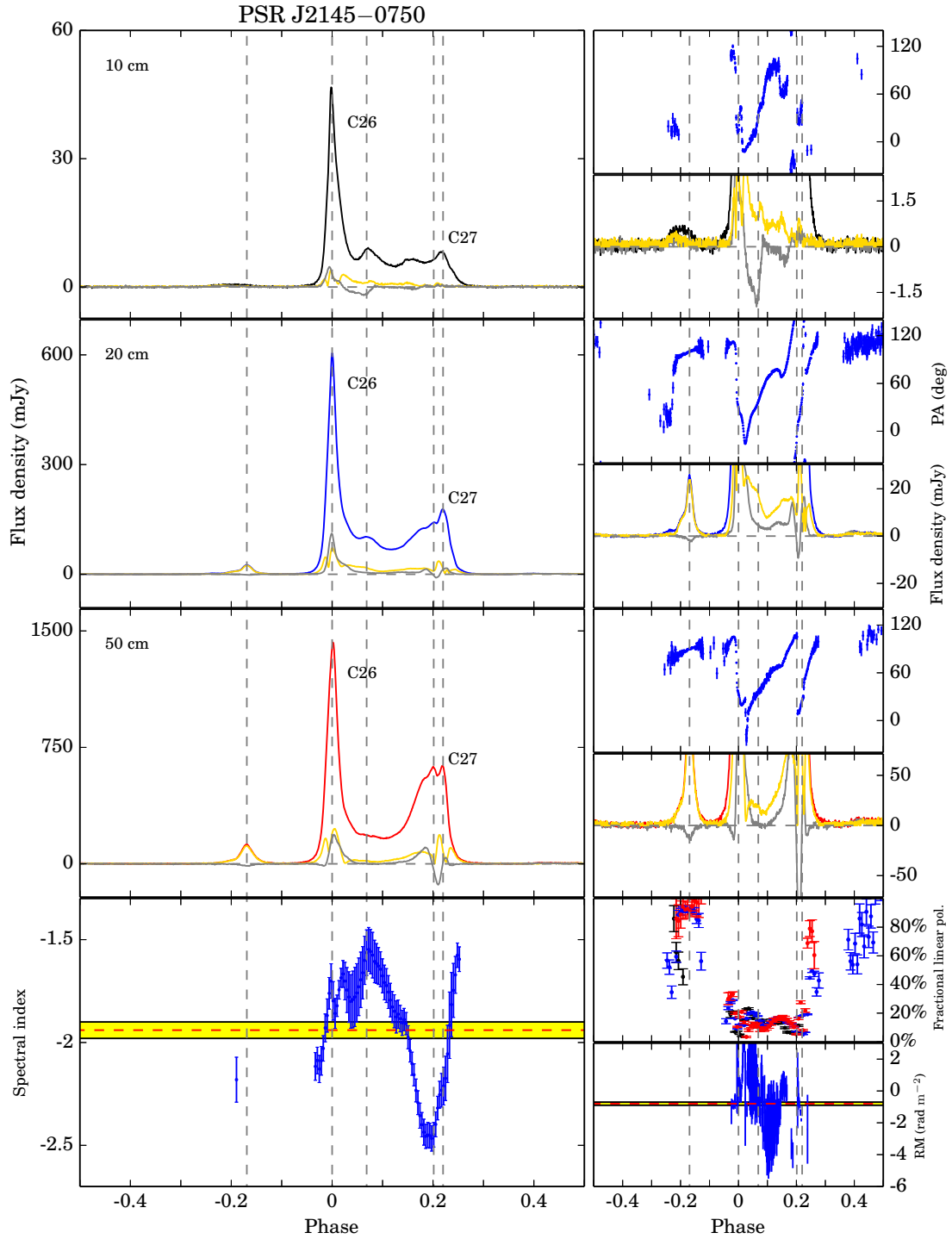


Figure A23. Multi-frequency polarization profiles for PSR J2145–0750. See Fig. A1 for further details.

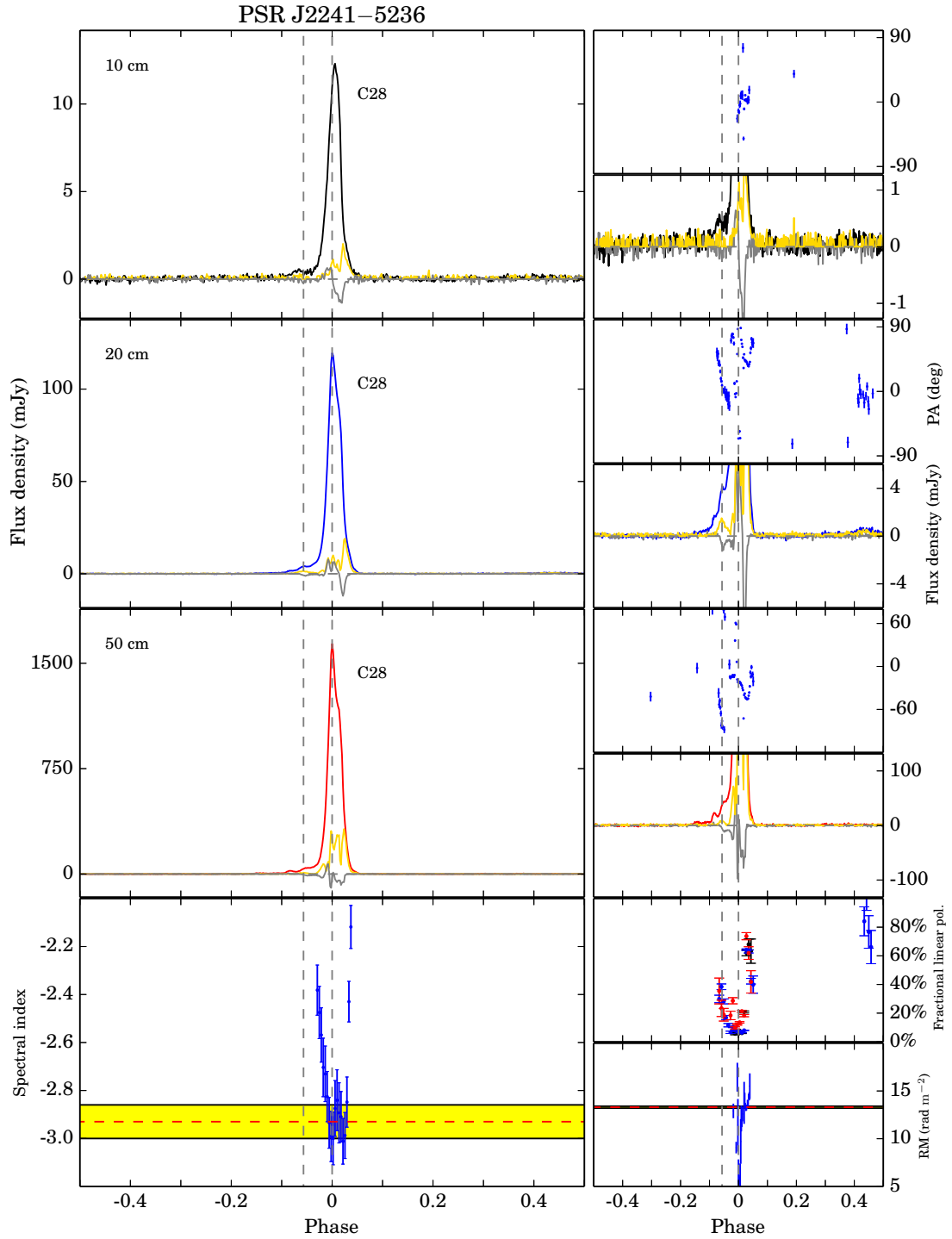


Figure A24. Multi-frequency polarization profiles for PSR J2241–5236. See Fig. A1 for further details.